PERGAMON

International Journal of Solids and Structures 37 (2000) 2005–2034

INTERNATIONAL JOURNAL OF SOLIDS and STRUCTURES

www.elsevier.com/locate/ijsolstr

Dynamic elastic–plastic buckling of circular cylindrical shells under axial impact

D. Karagiozova [a], Norman Jones [b,*]

[a] *Institute of Mechanics, Bulgarian Academy of Sciences, Acad. G. Bonchev St., Block 4, Sofia 1113, Bulgaria*
[b] *Impact Research Centre, The University of Liverpool, Brownlow Street, Liverpool L69 3GH, UK*

Received 15 July 1998; in revised form 11 November 1998

Abstract

Dynamic axisymmetric buckling of circular cylindrical shells struck axially by a mass is studied in order to clarify the initiation of buckling and to provide some insight into the buckling mechanism as a transient process. It is assumed that the material is elastic–plastic with linear strain hardening and displaying the Bauschinger effect. The deformation process is analysed by a numerical simulation using a discrete model. Particular attention is paid to the influence of stress wave propagation on the initiation of buckling. It is found that the development of the buckling shape depends strongly on the inertia properties of the striker and on the geometry of the shell. The theoretical method is used to clarify some experimental data and good agreement is obtained with results on aluminium alloy tubes.

Keywords: Dynamic buckling; Cylindrical shell; Axial impact; elastic–plastic; Stress waves

Nomenclature

a	initial mean radius of the actual shell
c	uniaxial elastic wave speed
c_1^{p}, c_2^{p}	plastic wave speeds, eqns (C9a,b)
$\boldsymbol{e}_s$	mean meridional strain vector, $[e_s^1, \ldots, e_s^{n+1}]^T$
e_s^i	mean meridional strain in the i-th cell, $e_s^i = (2n_t + 1)^{-1} \sum_{k=1}^{2n_t+1} \varepsilon_{s,k}^i$
E, E_{h}	Young's and hardening moduli, respectively
$F_{i\alpha}^s$	meridional force per unit hoop length in the i-th cell of the model, $\alpha = 1, \ldots, 2n_t + 1$

* Corresponding author. Tel.: +44-151-7944858; fax: +44-151-7944848.
E-mail address: njones@mechnet.liv.ac.uk (N. Jones).

0020-7683/00/$ - see front matter
PII: S0020-7683(98)00343-6

$F^{\theta}_{i\alpha}$ circumferential force per unit hoop length in the i-th cell of the model, $\alpha = 1, \ldots, 2n_t + 1$
$F^{r}_{i\alpha}$ radial force acting in the i-th cell of the model, $\alpha = 1, \ldots, 2n_t + 1$
g gravitational acceleration
G striking mass
h wall thickness of the actual shell and model
H' hardening parameter, (eqn (6b))
l length of the actual shell
L initial length of the i-th link
n number of the links of the model, $nL = l$
n_t $2n_t + 1 =$ number of the springs across the wall thickness
N^{s}_{i}, N^{θ}_{i}, M^{θ}_{i} meridional membrane force, circumferential membrane force and meridional bending moment per unit hoop length (eqn 2(a)–2(e)) in the i-th cell of the model, respectively
$P(t)$ axial load per unit hoop length at the impacted end
T_0 initial kinetic energy
$u_i(t)$ axial displacement of the model
v_0 initial velocity
$w_i(t)$ radial displacement of the model (taken positive outward).

Greek symbols

$\mathrm{d}\varepsilon_s$, $\mathrm{d}\varepsilon_\theta$ total strain increments
$\mathrm{d}\varepsilon^{\mathrm{p}}_s$, $\mathrm{d}\varepsilon^{\mathrm{p}}_\theta$ plastic strain increments
$\mathrm{d}\varepsilon_{\mathrm{p}}$ equivalent plastic strain increment, (eqn (6c))
δ_i shortening of the i-th link
Φ_{top}, Φ_{bottom} outer diameters corresponding to the maximum radial displacements near the ends $x = 0$ and $x = l$, respectively ($\Phi = 2(a + w) + h$)
φ_i angle of rotation of the i-th link
λ E_{h}/E
$\mathrm{d}\bar{\sigma}$ effective stress increment, (eqn (6a))
σ_0 yield stress
σ_{cr} static critical elastic stress of the actual shell, (eqn (12h))
$(\sigma^{\mathrm{c}}_s, \sigma^{\mathrm{c}}_\theta)$ co-ordinates of the origin of the Tresca hexagon (Fig. 2(c))
ν Poisson's ratio

1. Introduction

Thin-walled ductile metal tubes are used widely in industry, and their static and dynamic behaviour has been studied both theoretically and experimentally (see e.g. Florence and Goodier 1968; Wang Ren et al., 1983; Jones, 1989; Murase and Jones, 1991, 1993; Chen Changen et al., 1992; Li Ming et al., 1994; Lepik, 1998). In particular, axially crushed tubes have been examined in order to obtain the critical forces, types and modes of buckling and the energy absorbing properties, etc.

The experimentally obtained buckling shapes of dynamically loaded circular tubes, not only vary according to the geometry of the cross-section and the material properties, but they also depend on the experimental loading technique as shown by Florence and Goodier (1968), Wang Ren et al. (1983), Murase and Jones (1991, 1993), Chen Changen et al. (1992) and Li Ming et al. (1994). Moreover, a

complete description of the collapse process involves several stages. It is well known that a quasi-static load causes a tube to collapse by a progressive folding process for which the deformations occur locally, while high velocity impacts cause deformations to develop over the entire length of the tube due to inertia effects (Jones, 1989). However, because of the complexity of the problem, a detailed knowledge of the behaviour is not understood completely due to the difficulties in obtaining the stress profiles in thin-walled members. In particular, the initiation of the buckling mechanism as a transient process has received little attention since the theoretical studies of Lee (1981a, b), except for some recent results for cylindrical shells obtained by Lepik (1998) and rods reported by Karagiozova and Jones (1996a, b).

The experiments on aluminium alloy cylindrical shells reported by Chen Changen et al. (1992) and Li Ming et al. (1994) show some local buckling effects which are explained tentatively by stress wave effects. An analytical approach is used by Lepik (1998) to examine the development of the buckling process in an elastic–plastic cylindrical shell struck axially by a mass. However, the complexity of the problem has led to a number of simplifications in the theoretical analysis, which do not allow a comparison to be made between the theoretical predictions and the available experimental data. In particular, a static equilibrium state has been used to obtain the propagation of the flexural waves in the shell which is not appropriate for modelling transient processes.

The effects of stress wave propagation on the elastic–plastic buckling of a rod, subjected to an axial mass impact, is studied numerically using a discrete model by Karagiozova and Jones (1996a, b), where the theoretical predictions are shown to be in agreement with several experimental studies. It is shown that the inertia properties of the striking mass play an important role during the buckling process by initiating the propagation of different plastic waves along the rod which cause different buckling patterns (Karagiozova and Jones 1996b).

In the present paper, the dynamic response of circular cylindrical shells, which have different geometrical characteristics and are subjected to axial mass impacts having velocities between 6.26 m/s and 125.3 m/s, is analysed in order to clarify the influence of elastic and plastic stress waves on the initiation of buckling and to provide some insight into the post-buckling behaviour. Different loading conditions are modelled to clarify the influence of experimental loading techniques on the buckling process. This analysis is carried out numerically using a discrete model for the axisymmetric buckling of an elastic–plastic shell. The theoretical predictions are compared with the experimental data reported in the literature by Florence and Goodier (1968) and Murase and Jones (1993) and obtained recently in the Impact Research Centre at the University of Liverpool.

2. Types of loading conditions

Different experimental techniques create a variety of load-time histories, which are not known in advance, as they are a result of interaction between the loading device and the impacted structure. This increases the complexity of a buckling analysis. Moreover, the characteristics of a load-time history can influence the initiation of buckling.

In the present study, the dynamic elastic–plastic response of two specimen types is analysed in order to clarify the influence of the loading conditions on the buckling behaviour of circular cylindrical shells. It is assumed that the specimen in Fig. 1(a) is stationary and is impacted by a mass G travelling with an initial velocity v_0 (see Wang Ren et al., 1983; Chen Changen et al., 1992; Murase and Jones, 1993). Different combinations of the striking masses and initial velocities are examined in order to clarify the influence of the inertia properties of the striker on the buckling process and on the final buckled shape. The specimen in Fig. 1(b) with an attached mass G is impacted against a rigid wall (Florence and Goodier, 1968; Murase and Jones, 1993).

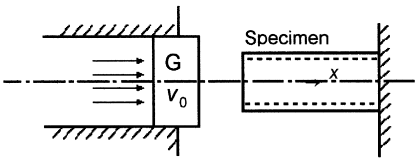

(a)

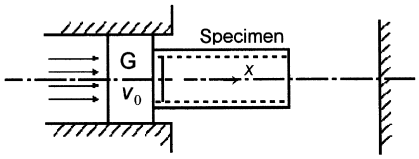

(b)

Fig. 1. Types of specimens: (a) stationary, (b) moving.

3. Discrete model for dynamic axisymmetric buckling of a circular cylindrical shell under axial impact

Ductile metal tubes with small radius-to-thickness ratios are known to collapse axisymmetrically when impacted axially so that, for the purpose of the following analysis, the shell can be divided into identical longitudinal strips. Each strip is assumed to carry the same axial load. In this case, the lumped mass model in Fig. 2(a, b) can be used to study the dynamic axisymmetric buckling of a circular cylindrical shell. It is assumed that the longitudinal axis of the idealised model coincides with the meridional axis of the actual shell. A similar procedure was used by the present authors to build a discrete model for the dynamic elastic–plastic buckling of a rod, subjected to various types of axial impacts (Karagiozova and Jones, 1996a, b), which gave good agreement between the model predictions and experimental data.

The model in Fig. 2(a, b) consists of n rigid (with respect to bending, but compressible) weightless links of length $L_i = L - \delta_i$ connected by springs, which simulate the elastic–plastic material properties, and where δ_i is the reduction in length of the i-th link. The springs across the thickness cater for the meridional membrane forces and the meridional bending moments, while the springs in the radial direction, model the circumferential membrane forces in an actual shell. The forces $F^s_{i\alpha}$ and $F^r_{i\alpha} = L_i F^\theta_{i\alpha}/(a + w_i)$ are associated with the meridional and the circumferential stresses, respectively, acting in α-th 'layer' through the shell thickness, where $\alpha = 1, \ldots, 2n_t + 1$ and n_t are associated with the integration points across the thickness. The thickness of the model is h. It is assumed that the total mass of the shell per unit initial hoop length m_1, is distributed as discrete masses $m = m_1/2n$ at each end of a link.

The proposed model with elastic–plastic springs (Fig. 2(a)), which idealise the actual material properties, has a yield condition for each layer in terms of the biaxial stresses, $\sigma_s(s, z)$ and $\sigma_\theta(s, z)$ in a shell subjected to an axial impact. This approach is more accurate than using a yield condition in terms of the generalised forces N_s, N_θ and M_s and allows for the development of the temporal stress–strain profiles of thin-walled tubes in order to clarify the buckling and post-buckling processes.

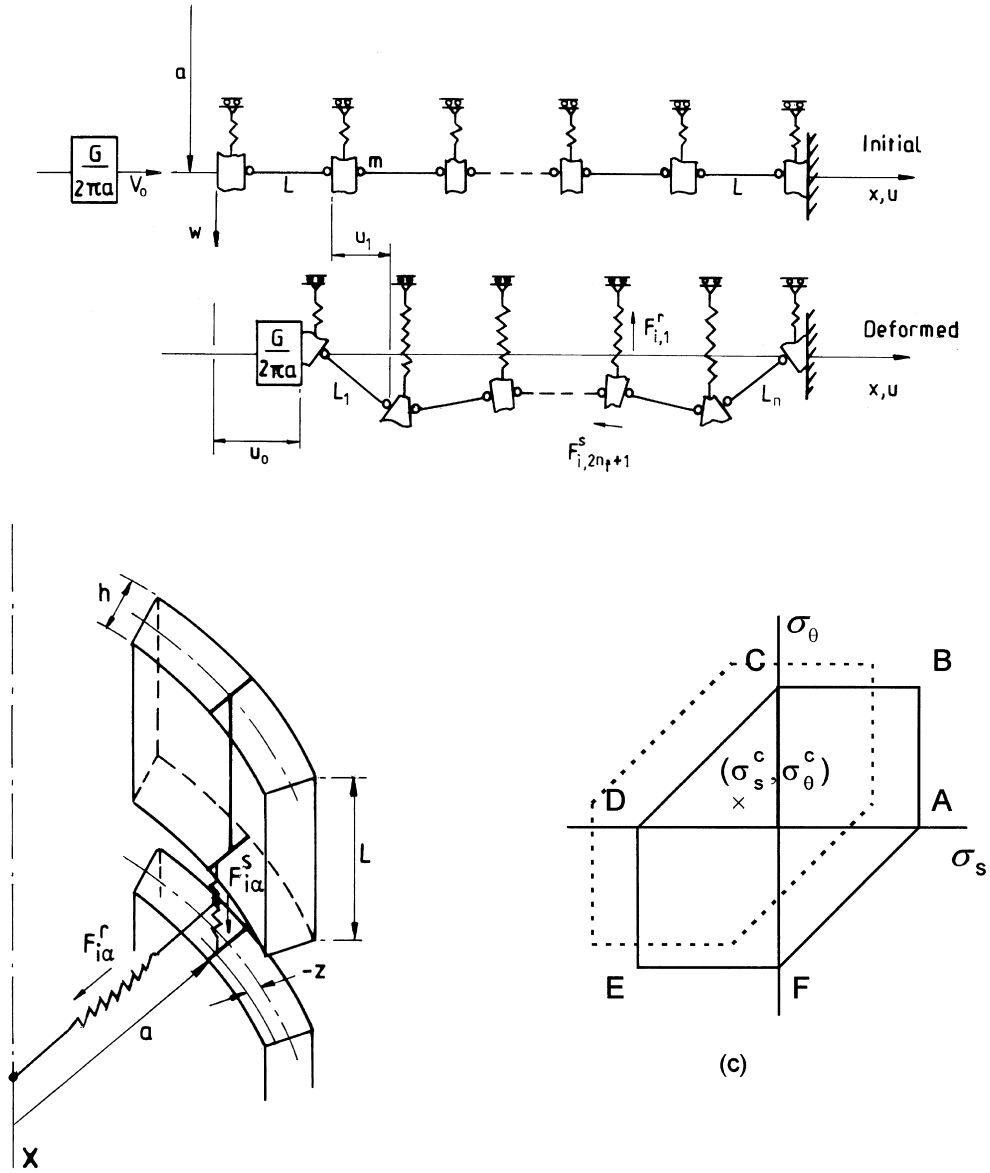

Fig. 2. (a) A discrete model for axisymmetric shell buckling (the radial force $F^r_{i,\alpha}$ is shown for the inner layer only); (b) a typical cell in the model; (c) yield locus for kinematic hardening.

3.1. Equations of motion

Large rotations of the links in Fig. 2(a, b) are permissible so that the equations of motion for the model are

$$G_1\ddot{u}_0 = N_0^x + G_1 g, \tag{1a}$$

$$
\begin{aligned}
s_1 m\ddot{u}_i = {} & N_i^s\Big\{\cos\alpha_i[2 + a_1(\sin\varphi_i - b_1) - a_2(\sin\varphi_{i+1} + d_1) - \sin\alpha_i\Big[a_1(\cos\varphi_i - b_2) \\
& - a_2(\cos\varphi_{i+1} + d_2)\Big]\Big\}/2 - N_{i-1}^s\{\cos\alpha_{i-1}[2 - a_1(\sin\varphi_i + b_1)] \\
& + a_2\sin\alpha_{i-1}(\cos\varphi_i + b_2)\}/2 - N_{i+1}^s a_2\{\cos\alpha_{i+1}(\sin\varphi_{i+1} - d_1) \\
& + \sin\alpha_{i+1}(\cos\varphi_{i+1} - d_2)\}/2 - N_{i-1}^r a_1(\cos\varphi_i + b_2)/4 \\
& + N_i^r\Big[a_1(\cos\varphi_i - b_2) + a_2(\cos\varphi_{i+1} + d_2)\Big]/4 \\
& - N_{i+1}^r a_2(\cos\varphi_{i+1} - d_2)/4 - a_1 M_{i-1}^s/L_i + M_i^s(a_1/L_i + a_2/L_{i+1}) \\
& - a_2 M_{i+1}^s/L_{i+1} + mf_1(\ddot{w}_{i-1}, \ddot{w}_i, \ddot{w}_{i+1}, \ddot{u}_{i-1}, \ddot{u}_{i+1}, \dot{w}_{i-1}, \dot{w}_i, \dot{w}_{i+1}, \dot{u}_{i-1}, \dot{u}_i, \dot{u}_{i+1}) \\
& + 2mg, \quad i = 1, \ldots, n-1,
\end{aligned}
\tag{1b}
$$

$$
\begin{aligned}
s_2 m L_i\ddot{w}_i = {} & M_{i-1}^s - M_i^s(1 + c_i L_i/L_{i+1}) + M_{i+1}^s c_i L_i/L_{i+1} - N_{i-1}^s L_i\big[\cos\alpha_{i-1}(\sin\varphi_i - e_1) \\
& - \sin\alpha_{i-1}(\cos\varphi_i - e_2)\big]/2 - N_i^s L_i\Big\{\cos\alpha_i\Big[(\sin\varphi_i + e_1) - c_i(\sin\varphi_{i+1} + d_1)\Big] \\
& - \sin\alpha_i\big[(\cos\varphi_i + e_2) - c_i(\cos\varphi_{i+1} + d_2)\big]\Big\}/2 + N_{i+1}^s L_i c_i\big[\cos\alpha_{i+1}(\sin\varphi_{i+1} - d_1) \\
& - \sin\alpha_{i+1}(\cos\varphi_{i+1} - d_2)\big]/2 + N_{i-1}^r L_i(\cos\varphi_i - e_2)/4 \\
& - N_i^r L_i\big[(\cos\varphi_i + c_i(\cos\varphi_{i+1} + d_2) + e_2)\big]/4 + N_{i+1}^r L_i c_i(\cos\varphi_{i+1} - d_2)/4 \\
& + mL_i f_2(\ddot{w}_{i-1}, \ddot{w}_{i+1}, \ddot{u}_{i-1}, \ddot{u}_i, \ddot{u}_{i+1}, \dot{w}_{i-1}, \dot{w}_i, \dot{w}_{i+1}, \dot{u}_{i-1}, \dot{u}_i, \dot{u}_{i+1}), \quad i = 2, \ldots, n-2,
\end{aligned}
\tag{1c}
$$

where $\alpha_i = (\varphi_i + \varphi_{i+1})/2$ and $N_i^r = N_i^\theta L_i/(a + w_i)$. The coefficients $a_1, a_2, b_1, b_2, c_i, d_1, d_2, e_1, e_2, s_1, s_2$ are functions of the angles of rotation φ_i and their expressions are given in Appendix A together with the equations of motion for w_1, w_{n-1} and u_n which take into account the particular boundary conditions. In eqn (1), $G_1 = G/2\pi a$, G is the striking mass, g is the gravitational acceleration (taken into account in the case of a drop mass impact), u_i is the total axial displacement, φ_i, is the rotation of the i-th link and the radial displacements, w_i, (taken positive in the outward direction) are referred to the model parameters as $w_i - w_{i-1} = L_i \sin\varphi_i$. The model can incorporate stress-free initial axisymmetric imperfections, $\bar{w}_i - \bar{w}_{i-1} = L\sin\bar{\varphi}_i$, but they are not examined in the present study. The generalised stresses N_i^s, N_i^θ and M_i, are the respective meridional membrane force, circumferential membrane force and meridional bending moment per unit hoop length in the i-th cell and are obtained when integrating the biaxial stress field across the thickness as

$$
\mathrm{d}F_{ik}^s = \frac{h}{(2n_t + 1)}\,\mathrm{d}\sigma_{ik}^s, \quad \mathrm{d}N_i^s = \sum_{k=1}^{2n_t+1}\mathrm{d}F_{ik}^s,
$$

$$
\mathrm{d}F_{ik}^\theta = \frac{h}{(2n_t + 1)}\,\mathrm{d}\sigma_{ik}^\theta, \quad \mathrm{d}N_i^\theta = \sum_{k=1}^{2n_t+1}\mathrm{d}F_{ik}^\theta,
$$

$$\mathrm{d}M_i^s = \cos\left[(\varphi_{i-1}+\varphi_{i+1})/2\right]\frac{h}{2n_t}\sum_{k=1}^{2n_t+1}(k-n_t-1)\,\mathrm{d}F_{ik}^s. \tag{2a)–(2e)}$$

It can be shown that eqn (1) reduces to (Jones, 1989)

$$\frac{\partial N_x}{\partial x}-\rho h\frac{\partial u^2}{\partial t^2}=0,$$

$$\frac{\partial^2 M_x}{\partial x^2}+\frac{\partial}{\partial x}\left\{N_x\left(\frac{\partial w}{\partial x}+\frac{\partial \bar{w}}{\partial x}\right)\right\}+\frac{N_\theta}{a}-\rho h\frac{\partial^2 w}{\partial t^2}=0$$

for small displacements (w is taken as positive in the inward direction for these equations only), where ρ is the material density.

The initial conditions for the problems studied in this article are

$$\begin{aligned} &u_i(0)=0,\ i=0,\ldots,n,\quad \dot{u}_0(0)=v_0,\quad \dot{u}_i(0)=0,\ i=1,\ldots,n,\\ &w_i(0)=\dot{w}_i(0)=0,\ i=0,\ldots,n \end{aligned} \tag{3a)–(3d)}$$

for a stationary specimen in Fig. 1(a) when struck by a mass G travelling with an initial velocity v_0 at the end $i=0$, and

$$\begin{aligned} &u_i(0)=0,\ i=0,\ldots,n,\quad \dot{u}_i(0)=v_0,\ i=0,\ldots,n-1,\quad \dot{u}_n(0)=0,\\ &w_i(0)=\dot{w}_i(0)=0,\ i=0,\ldots,n \end{aligned} \tag{3e)–(3h)}$$

for a moving specimen in Fig. 1(b) travelling with an initial velocity v_0 and striking a rigid boundary at $i=n$. Clamped boundary conditions with respect to the radial displacements are considered for both specimen types

$$w_0=\bar{w}_0=0 \tag{4a}$$

$$w_n=\bar{w}_n=0 \tag{4b}$$

when $M_0^s(t)\neq 0$ and $M_n^s(t)\neq 0$. It is assumed for the clamped-clamped case that the end $x=l=nL$ is stationary, while the end $x=0$ ($i=0$) can move axially.

3.2. Constitutive equations

An elastic–plastic, strain rate insensitive material with linear strain hardening and displaying the Bauschinger effect is considered in this article. It is assumed that the material obeys the Tresca yield criterion. This is consistent with previous studies carried out by Sewell (1973) on the influence of the yield criterion on the critical buckling load which show that piece-wise linear surfaces give better estimates for the critical load than the von Mises yield criterion which predicts values higher than the corresponding experimental ones.

It is assumed that the strain increments are divided into elastic and plastic parts so that the total increments are

$$\mathrm{d}\varepsilon_s=\mathrm{d}\varepsilon_s^{\mathrm{p}}+(\mathrm{d}\sigma_s-\nu\,\mathrm{d}\sigma_\theta)/E,$$

$$\mathrm{d}\varepsilon_0 = \mathrm{d}\varepsilon_\theta^{\mathrm{p}} + (\mathrm{d}\sigma_\theta - \nu\,\mathrm{d}\sigma_s)/E,$$

$$\mathrm{d}\varepsilon_z^{\mathrm{p}} = -\left(\mathrm{d}\varepsilon_s^{\mathrm{p}} + \mathrm{d}\varepsilon_\theta^{\mathrm{p}}\right). \tag{5a)–(5c)}$$

The effective stress increment, $d\bar{\sigma}$, satisfies the relation

$$\mathrm{d}\bar{\sigma} = H'\,\mathrm{d}\varepsilon_{\mathrm{p}}, \tag{6a}$$

$$H' = EE_{\mathrm{h}}/(E - E_{\mathrm{h}}) = \lambda E/(1-\lambda) \tag{6b}$$

for a linear strain hardening material, where the equivalent plastic strain increment, $\mathrm{d}\varepsilon_{\mathrm{p}}$, is

$$\mathrm{d}\varepsilon_{\mathrm{p}} = 2\left[\left(\mathrm{d}\varepsilon_s^{\mathrm{p}}\right)^2 + \left(\mathrm{d}\varepsilon_\theta^{\mathrm{p}}\right)^2 + \left(\mathrm{d}\varepsilon_s^{\mathrm{p}}\right)\left(\mathrm{d}\varepsilon_\theta^{\mathrm{p}}\right)\right]^{1/2}/\sqrt{3}, \tag{6c}$$

for an incompressible material and axisymmetric behaviour. The total strains, $\varepsilon_s(z)$ and ε_θ for an actual shell are modelled by the spring displacements in the model cells as

$$\varepsilon_s^i(z) = -\delta_i/L - 4z\sin\left[(\varphi_i - \varphi_{i-1})/2\right]/(L_{i-1} + L_i) \tag{7a}$$

$$\varepsilon_\theta^i = w_i/a, \tag{7b}$$

where

$$\delta_i = L - \left[(w_i - w_{i-1})^2 + (L + u_i - u_{i-1})^2\right]^{1/2} \tag{7c}$$

and for small angles eqn (7a) reduces to

$$\varepsilon_x = \frac{\partial u}{\partial x} - z\frac{\partial^2 w}{\partial x^2} + \frac{1}{2}\left(\frac{\partial w}{\partial x}\right)^2 + \frac{1}{2}\left(\frac{\partial u}{\partial x}\right)^2 \tag{7d}$$

when assuming $L = \Delta x$ and $\Delta x \to 0$.

In the above equations, E is Young's modulus and E_{h} is the hardening modulus. In this case, explicit expressions for the stress increments as functions of the strain increments and the material properties can be obtained for elastic loading and elastic unloading and for the plastic loading associated with each side of the Tresca diagram (Fig. 2(c)) as

$$\mathrm{d}\sigma_s = f_3(\mathrm{d}\varepsilon_s, \mathrm{d}\varepsilon_\theta, \nu, E, \lambda) \tag{8a}$$

$$\mathrm{d}\sigma_\theta = f_4(\mathrm{d}\varepsilon_s, \mathrm{d}\varepsilon_\theta, \nu, E, \lambda), \tag{8b}$$

where ν is Poisson's ratio (see Appendix B). The force-time history is a result of interaction between the applied load and the response of the specimen, so that an explicit integration procedure is required (Karagiozova and Jones, 1996a, b).

It is known that the axial compression and bending phases of deformation can be distinguished in many elastic–plastic buckling problems. This phenomenon leads to complex loading paths at each point of a structure, particularly for strain hardening materials. In the present paper, a kinematic hardening rule is assumed, which allows for a translation of the Tresca hexagon without any distortion of the elastic range where the velocity of the yield locus is proportional to the plastic strain rates (Prager's

hardening rule). The discrete model in Fig. 2(a) requires $(n+1)\times(2n_t+1)$ components of σ_s and σ_θ, so that $(n+1)\times(2n_t+1)$ yield loci associated with the loading paths are analysed at each time step. The temporal movement of the Tresca hexagon in the plane $(\sigma_s, \sigma_\theta)$, which is identified by the variation of its centre $(\sigma_s^c, \sigma_\theta^c)$ (Fig. 2(c)), can be associated with the loading path of each layer in a shell cross-section.

If $\boldsymbol{F}_j[(\sigma_s, \sigma_\theta), (\sigma_s^c, \sigma_\theta^c)], j=1,\ldots,6$ is a system of functions which determine the six sides of the Tresca yield locus, then elastic loading occurs when all $\boldsymbol{F}_j[(\sigma_s, \sigma_\theta), (\sigma_s^c, \sigma_\theta^c)]<0$. Now

$$\boldsymbol{F}_j\left[(\sigma_s, \sigma_\theta), \left(\sigma_s^c, \sigma_\theta^c\right)\right]=0, \quad \dot{\boldsymbol{F}}_j>0, \quad \frac{\partial \boldsymbol{F}_j}{\partial \sigma_s}\dot{\sigma}_s+\frac{\partial \boldsymbol{F}_j}{\partial \sigma_\theta}\dot{\sigma}_\theta>0, \quad \dot{\varepsilon}_p\neq 0, \tag{9a–9d}$$

for active plastic loading,

$$\boldsymbol{F}_j\left[(\sigma_s, \sigma_\theta), \left(\sigma_s^c, \sigma_\theta^c\right)\right]=0, \quad \dot{\boldsymbol{F}}_j=0, \quad \frac{\partial \boldsymbol{F}_j}{\partial \sigma_s}\dot{\sigma}_s+\frac{\partial \boldsymbol{F}_j}{\partial \sigma_\theta}\dot{\sigma}_\theta=0, \quad \dot{\varepsilon}_p=0, \tag{10a–10d}$$

for neutral plastic loading and

$$\boldsymbol{F}_j\left[(\sigma_s, \sigma_\theta), \left(\sigma_s^c, \sigma_\theta^c\right)\right]=0, \quad \frac{\partial \boldsymbol{F}_j}{\partial \sigma_s}\dot{\sigma}_s+\frac{\partial \boldsymbol{F}_j}{\partial \sigma_\theta}\dot{\sigma}_\theta<0, \quad \dot{\varepsilon}_p=0, \tag{11a–11c}$$

for elastic unloading.

3.3. Method of solution

The initial value problem stated by eqns (1)–(3) is highly non-linear due to the material and the geometrical nonlinearities. It is integrated numerically using the D0EAF-NAG FORTRAN Library Routine for a system of first order ordinary differential equations using a variable order, variable step method implementing the Backward Differentiation Formulae (BDF). This method of integration allowed the required accuracy to be maintained during the entire response of the model. The following non-dimensional variables are used when integrating eqns (1)–(3)

$$y_i=u_i/L, \quad \zeta_i=2w_i/h, \quad \bar{\zeta}_i=2\bar{w}_i/h, \quad \bar{\delta}_i=\delta_i/L, \quad \bar{N}_i^s=2N_i^s/\sigma_{cr}h, \quad \bar{N}_i^\theta=2N_i^\theta/\sigma_{cr}h,$$
$$\bar{M}_i^s=2M_i^s/\sigma_{cr}h^2, \quad \sigma_{cr}=Eh\left[3(1-\nu^2)\right]^{-1/2}/a, \quad \tau=t(E_h/\rho)^{1/2}/l. \tag{12a–12i}$$

The axial force, acting on the end of a shell, $P(t)$, and the stresses in the shell wall σ_s, σ_θ, are discussed further in terms of the dimensionless variables

$$\bar{P}(\tau)=2P(t)/h\sigma_{cr} \quad q_s=\sigma_s/\sigma_{cr}, \quad q_\theta=\sigma_\theta/\sigma_{cr}, \tag{13a–13c}$$

where σ_{cr} is defined by eqn (12h) and is the critical elastic buckling stress for axisymmetric buckling of an actual shell.

The numerical calculations presented in this paper are obtained with a dimensionless time step $\Delta\tau=0.00005$ which is to be compared with a dimensionless time of $1900\Delta\tau=0.095$ which is required for an elastic wave to propagate along one length of the shell for the particular material properties given in Section 4.

Due to the severe loading conditions, large deformations can develop during the response. In such cases, non-penetration conditions should be employed at the shell wall and at the edges of a shell. The

contact problem arising from these conditions is complicated (see e.g. Benson and Hallquist, 1990), but because of the spring-mass discretisation of the shell, a simple non-penetration algorithm is used in this paper.

It is assumed that the shell walls can only touch which leads to the condition that the equations of motion eqn (1), are valid only when the distance between the axial co-ordinates of two non-neighbouring points, (y_i, ζ_i), is not less than the shell thickness. If wall touching occurs at points j and $j+k$, then deformation ceases in that part of the shell between j and $j+k$, but that part of the shell continues to move as a rigid body, so that

$$\dot{y}_i = \dot{y}_j, \quad i = j, \ldots j+k \tag{14a}$$

$$\dot{\zeta}_i = 0, \quad i = j, \ldots j+k. \tag{14b}$$

The condition for non-penetration of the edges of the shell is assured when assuming that the shell cannot go through the supports. Thus, if the axial displacements, y_i, near the supports of the shell ($i = l, \ldots, k$ and/or $i = n-1-k, \ldots, n-1$) reach the values of the support coordinates, y_0 or y_n, they continue to move axially with the axial velocities of the supports, while the radial velocities become zero, i.e.

$$\dot{y}_i = \dot{y}_0, \quad i = 1, \ldots k, \tag{15a}$$

$$\dot{\zeta}_i = 0, \quad i = 1, \ldots, k, \tag{15b}$$

and/or

$$\dot{y}_i = \dot{y}_n, \quad i = n-1-k, \ldots, n-1 \tag{16a}$$

$$\dot{\zeta}_i = 0, \quad i = n-1-k, \ldots, n-1, \tag{16b}$$

where k is the number of the shell points which are in contract with the support wall.

4. Comparison with experimental results

In this section, the model presented in Fig. 2 is verified for several types of loading which generate different buckling modes. The buckling shapes predicted by the model are compared with some new experimental data and with that reported by Florence and Goodier (1968) and Murase and Jones (1993). The numerical calculations are carried out for an aluminium alloy A1 6061-T6 having Young's modulus $E = 69$ GPa, hardening modulus $E_h = 690$ MPa and a yield stress $\sigma_0 = 310$ MPa.

4.1. Low velocity impact on a stationary specimen

The experiments discussed in this section were obtained on stationary vertical tubes which were placed on the anvil of a drop hammer rig in the Impact Research Centre at the University of Liverpool. The specimens have a length $l = 76.2$ mm, outer diameter 25.4 mm and thicknesses $h_A = 2.41$ mm, $h_B = 1.65$ mm and $h_C = 0.89$ mm (Specimens A, B and C, respectively) and were struck on the free end by a heavy mass G having an initial velocity v_0. The force-time histories and the final buckled shapes predicted by

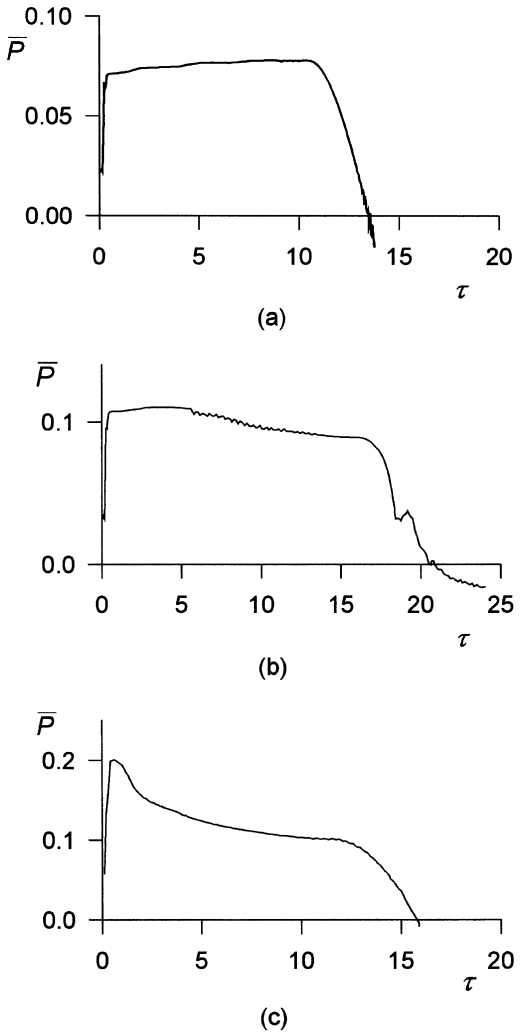

Fig. 3. Force-time histories (stationary specimens): (a) specimen A, $a = 11.495$ mm, $h = 2.41$ mm, $l = 76.2$ mm, $G = 12.2$ kg, $v_0 = 7.25$ m/s, $n = 50$, $n_t = 3$; (b) specimen B, $a = 11.875$ mm, $h = 1.65$ mm, $l = 76.2$ mm, $G = 12.2$ kg, $v_0 = 7$ m/s, $n = 50$, $n_t = 3$; (c) specimen C, $a = 12.255$ mm, $h = 0.89$ mm, $l = 76.2$ mm, $G = 3.7$ kg, $v_0 = 6.26$ m/s, $n = 60$, $n_t = 2$.

the model are shown in Figs. 3 and 4, respectively. It is evident from Fig. 3 that the applied forces acting on the three specimens have a finite rise time and that the compressive deformation of specimen A in Fig. 3(a) has an almost rectangular pulse shape. A localisation of the deformations, which form the folds near the impacted end, is a general feature of the deformed shapes in Fig. 4. It is evident that the thickest shell is deformed mainly in compression, while the $h = 1.65$ mm and $h = 0.89$ mm thick specimens respond with an axial compression and a local buckling near the impacted end with the remainder of the shell largely undeformed.

A comparison between the experimental data and the present predictions are presented in Table 1. It is evident that reasonable agreement is obtained for the axial shortening (δ_y) and for the maximum final outside tube diameters (Φ_{top}, Φ_{bottom}) near the supports.

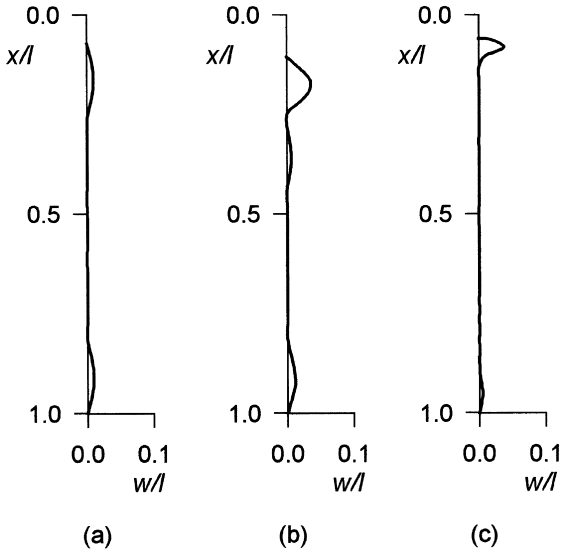

Fig. 4. Final buckled shapes: (a) specimen A; (b) specimen B; (c) specimen C.

4.2. High velocity impact on a stationary specimen

Specimen M38 in Murase and Jones (1993) has length $l = 101.6$ mm, mean radius $a = 11.875$ mm and thickness $h = 1.65$ mm and is struck axially by mass $G = 0.106$ kg travelling with an initial velocity $v_0 = 97$ m/s (Fig. 1(a)). The predicted final shape of the specimen is presented in Fig. 5(a) from which it is evident that the entire length is deformed almost regularly except for large local deformations near the stationary end. A similar deformed shape is observed experimentally with an axial shortening of 13 mm and maximum radial displacements giving $\Phi_{\text{bottom}} = 31$ mm, which compares with the predicted values of $\delta_y = 12.7$ mm and $\Phi_{\text{bottom}} = 30.95$ mm. The impact force is applied suddenly to the specimen and then decreases with time (Fig. 5(b)). It is shown by Karagiozova and Jones (1996b) that this type of loading force is due to the inertia properties of the striker.

4.3. High velocity impact of a shell on a rigid wall

The specimen shown in Fig. 1(b) is impacted against a rigid wall and is deformed between the wall and the mass attached to one end of the shell (Florence and Goodier, 1968). The shell and the mass

Table 1
Comparison between the experimental data and the model predictions for low velocity impact (drop mass impact)

	Experiment			Model predictions		
Specimen	δ_y (mm)	Φ_{top} (mm)	Φ_{bottom} (mm)	δ_y (mm)	Φ_{top} (mm)	Φ_{bottom} (mm)
A	5.8	26.69	26.61	5.54	26.91	26.80
B	8.35	30.72	26.42	8.09	31.14	27.10
C	6.55	29.05/ 30.85	26.42	6.21	31.42	26.15

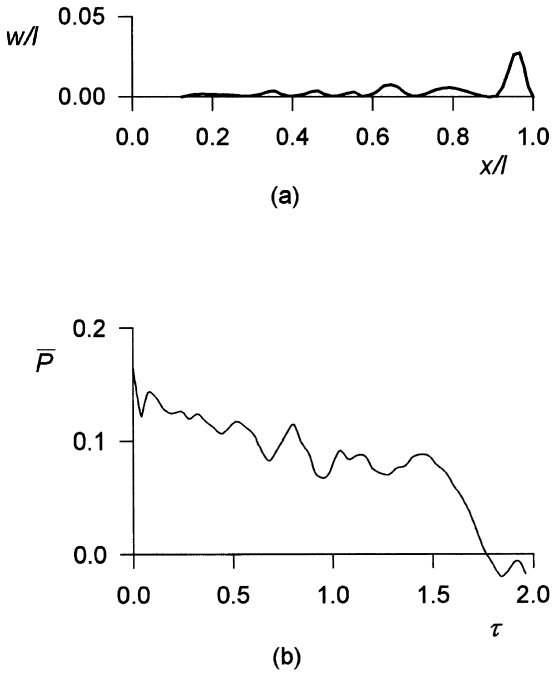

Fig. 5. Dynamic response of specimen M38 (Murase and Jones, 1993) (stationary): 11.875 mm, $h = 1.65$ mm, $l = 101.6$ mm, $G = 0.106$ kg, $v_0 = 97$ m/s, $n = 60$, $n_t = 3$. (a) Final buckled shape; (b) force-time history.

have equal velocities at $t = 0$, but the impacted end is stopped at $t_+ = 0$. Typical force-time histories for $\bar{P}(l, \tau)$, at the interface between the rigid target and a thick shell, and the force, $\bar{P}(0, \tau)$, acting on the attached mass, are shown in Fig. 6(a). The shape of the pulse, caused by the interaction between the shell and the rigid target, is similar to the pulse presented in Fig. 3(a), but in the current case of a high velocity impact, the force is applied more rapidly to the shell. The force $\bar{P}(0, \tau)$ is initiated by the reflected stress wave from the attached mass so that it is zero until $\tau = 0.095$. The buckled shapes for two relatively thick shells, which correspond to the specimens identified as tubes 4 and 13 in Florence and Goodier (1968), are presented in Fig. 6(b, c). Tube 4 has $l = 76.2$ mm, $a = 11.495$ mm and $h = 2.41$ mm and tube 13 has the same cross-section but $l = 101.6$ mm. Regular shapes are observed for both shells having almost equal wave lengths with the wave number depending on the shell length. The final experimental buckled profile of tube 4 (Florence and Goodier, 1968) is presented by a dashed line in Fig. 6(b). The calculated response time (the duration of the impact event) and the axial shortening, δ_y, are compared with the corresponding experimental values obtained by Florence and Goodier (1968) in Table 2 (all specimens have an outer diameter of 25.4 mm). It is evident that the proposed shell model provides reasonable estimates for δ_y but overestimates the duration of the impact event.

An impact of a moving specimen impacting a rigid wall, as shown in Fig. 1(b), is modelled for a shell having $l = 101.6$ mm, $a = 11.875$ mm and $h = 1.65$ mm when the initial velocity is 81 m/s and the attached mass is 0.114 kg (M4 in Murase and Jones, 1993). The predicted axial shortening is 12.3 mm, while the corresponding experimental value for δ_y is 14 mm. The final buckled shape for this specimen is presented in Fig. 6(d). It is evident that, although the impact conditions for the last two examples in Fig. 6(c, d) are similar, the thinner shell M4 in Fig. 6(d) responds with large local plastic deformations near the shell wall in contact with the target. The predicted values for the radial displacements give $\Phi_{\text{bottom}} = 31.1$ mm which compares favourably with the corresponding experimental value of $\Phi_{\text{bottom}} = 32$ mm.

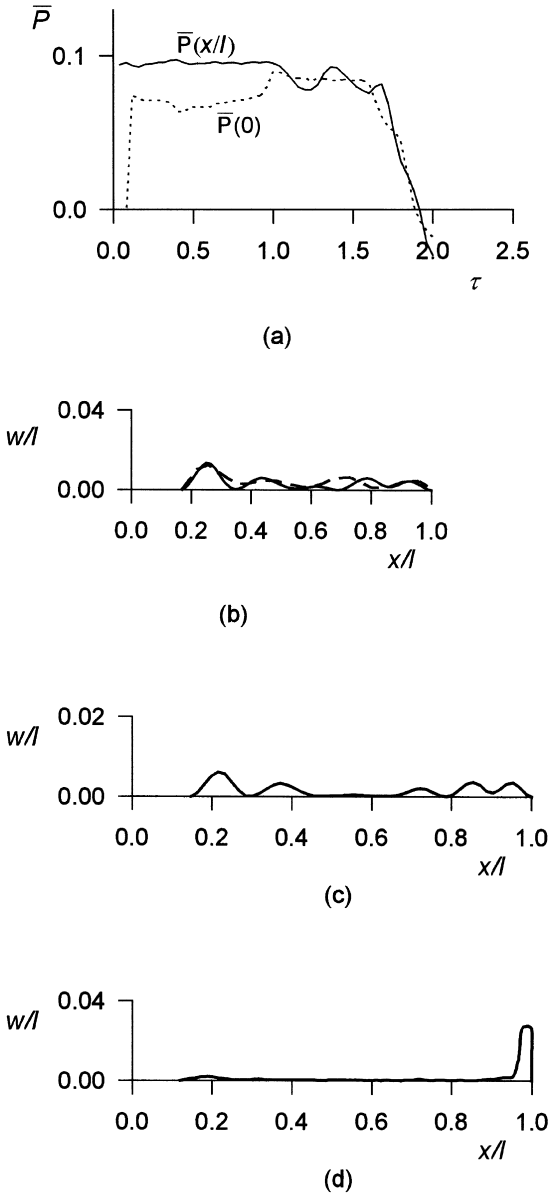

Fig. 6. Final buckled shapes for moving specimens: (a) force-time history for tube 4 (Florence and Goodier, 1968): $a = 11.495$ mm, $h = 2.41$ mm, $l = 76.2$ mm, $G = 0.127$ kg, $v_0 = 101.3$ m/s, $n = 50$, $n_t = 4$; (b) Final buckled shape of tube 4 (Florence and Goodier, 1968): $n = 50$, $n_t = 4$, - - - experiment (Florence and Goodier, 1968), — model prediction; (c) final buckled shape of tube 13 (Florence and Goodier, 1968): $a = 11.495$ mm, $h = 2.41$ mm, $l = 101.6$ mm, $G = 0.127$ kg, v_0 101.6 m/s, $n = 60$, $n_t = 3$; (d) final buckled shape of specimen M4 (Murase and Jones, 1993): $a = 11.875$ mm, $h = 1.65$ mm, $l = 101.6$ mm, $G = 0.114$ kg, $v_0 = 81$ m/s, $n = 50$, $n_t = 3$.

Table 2
Comparison between the experimental data (Florence and Goodier, 1968) and the model predictions for high velocity impact (moving specimen)

					Experiment Florence and Goorier (1968)		Model prediction	
Specimen	Attached mass (g)	h (mm)	l (mm)	v_0 (m/sec)	δ_y(mm)	duration (μsec)	δ_y (mm)	duration (μsec)
Tube 4	127	2.41	76.2	101.3	13.9	260	13.1	288
Tube 13	127	2.41	101.6	104.3	13.9	269	14.7	316
Tube 17	120	2.54	101.6	120.5	17.3	271	17.9	320
Tube 20	120	2.54	101.6	125.3	19.8	286	19.2	330
Tube 22	300	2.41	152.4	75	15.5	432	16.9	510

The results presented in this section show that large local deformations can be observed for both low (Fig. 4(b, c)) and high (Fig. 6(d)) velocity impacts, while for high velocity impacts, regular buckling shapes can develop for both moving (Fig. 6(b, c)) and stationary (Fig. 5(a)) shells. Moreover, different buckling shapes are generated when changing the geometry of the shell but maintaining similar loading and boundary conditions (Figs. 6(c) and 6(d)). Clearly, the buckling phenomenon is governed by the whole complex of loading parameters, boundary conditions and the geometrical characteristics of the specimens, so that the interaction between all impact parameters should be considered in any particular case.

5. Relation between the buckling shapes and stress wave phenomena

The local effects observed near the supports of some of the shells examined in Section 4 suggest that the buckling phenomenon is influenced significantly by stress wave propagation effects. The experimentally observed local buckling effects (Chen Changen et al., 1992; Li Ming et al., 1994) for shells made of two kinds of aluminium alloys also have been explained tentatively by stress wave effects, but without any quantitative explanation of the observed phenomena. It was shown by Karagiozova and Jones (1996b) that there is a strong relationship between the initiation of buckling and the elastic and plastic stress waves travelling along a rod, so that a similar type of behaviour is anticipated for axially loaded tubes.

It is shown in Appendix C (see eqn (C9)) that one elastic and two plastic stress wave speeds are possible in an elastic–plastic thin-walled tube with plastic flow governed by the Tresca yield condition. The elastic loading wave propagates with a speed $c^e = \{E/[\rho(1-\nu^2)]\}^{1/2}$ and the plastic waves can propagate with two different velocities, namely

$$c_1^p = \pm(E/\rho)^{1/2}\left\{2\lambda/\left[2\lambda(1-\nu^2)+(1-\lambda)\sqrt{3}\right]\right\}^{1/2}$$

and

$$c_2^p = \pm(E/\rho)^{1/2}\left\{\frac{2\lambda+(1-\lambda)\sqrt{3}}{2(1-\nu)\left[\lambda(1+\nu)+(1-\lambda)\sqrt{3}\right]}\right\}^{1/2},$$

depending on the stress state. The plastic wave speed c_2^p is associated with the sides CD and FA of the Tresca hexagon in Fig. 2(c), while c_1^p is associated with the other sides.

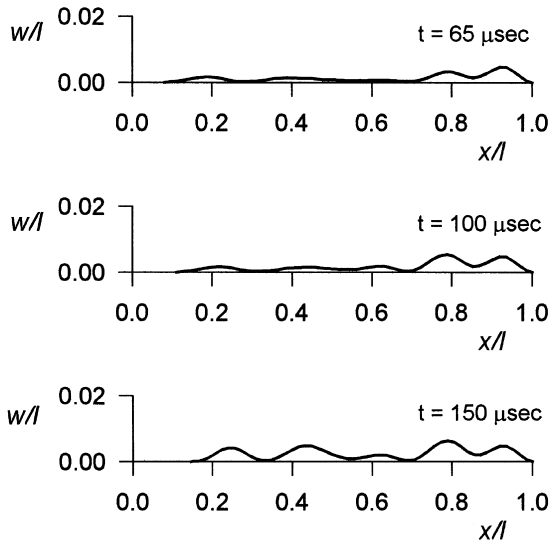

Fig. 7. Development of the buckling shape for Tube 4 (Florence and Goodier, 1968): $n = 50$, $n_t = 4$.

5.1. Stress wave phenomena in a moving specimen

The temporal development of the buckling shape for the shell presented in Fig. 6(b) and predicted by the model at 65, 100 and 150 μs after impact, is shown in Fig. 7. The associated axial shortenings are 7.8, 11.4 and 15.1%, while the corresponding experimental values (Florence and Goodier, 1968) are 7.2, 12.5 and 14.5%, respectively. The preferred mode at 65 μs in Fig. 7 is consistent with the experimental results which show that the shell commences to buckle from the impacted end. The meridional strain distributions along the longitudinal axis and across the thickness of the shell at $t = 65$ μs are shown in Fig. 8(a), while Figs. 8(b) and 8(c) present the movement of the centre of the Tresca hexagon in the s and θ directions, respectively.

The position of the yield loci, q_s^c, shows that the movement in the s direction is much larger than the movement in the θ direction, which, therefore, indicates an almost uniaxial stress state on the side DE of the Tresca hexagon. At $t = 65$ μs, the plastic wave travelling with a speed c_1^p has reached a distance $0.458l$ from the impacted end ($x = l$). However, an analysis of Fig. 8(b, c) shows that, although very small, plastic deformations have developed along the entire length of the shell, as indicated by the movement of the yield loci from their origins (0, 0). This effect is due to the circumferential forces which cause a loading path associated with the side CD of the yield condition compression in the axial direction and tension in the circumferential direction, (Fig. 2(c)) shortly after the impact. This plastic wave which has a speed $c_2^p > c_1^p$ overtakes the initial plastic wave travelling at a speed c_1^p and the two plastic waves become distinct at $t = 0.35$ μs ($\tau = 0.00233$). It should be noted that the faster moving stress wave with a speed c_2^p has small associated plastic strains, while large plastic strains are associated with the slower moving stress wave with a speed c_1^p (Fig. 8(a, d)). The slower plastic wave propagates one length of the tube in 142 μs ($\tau = 0.932$), while the corresponding time for the faster plastic wave is 18 μs ($\tau = 0.118$). Fig. 8(b, c) indicates also, that the elastic wave travelling from $x = l$ has reflected from $x = 0$ as a plastic one at $t = 14.5$ μs ($\tau = 0.0954$) and at $t = 65$ μs has travelled a distance $0.355l$ from the moving end with a speed c_1^p. However, the small inertial resistance of the attached mass ($G = 0.127$ kg) cannot cause significant plastic strains. Nevertheless, buckling is also evident near the moving end ($x = 0$) along the distance covered by the reflected plastic wave (Fig. 7, $t = 65$ μs).

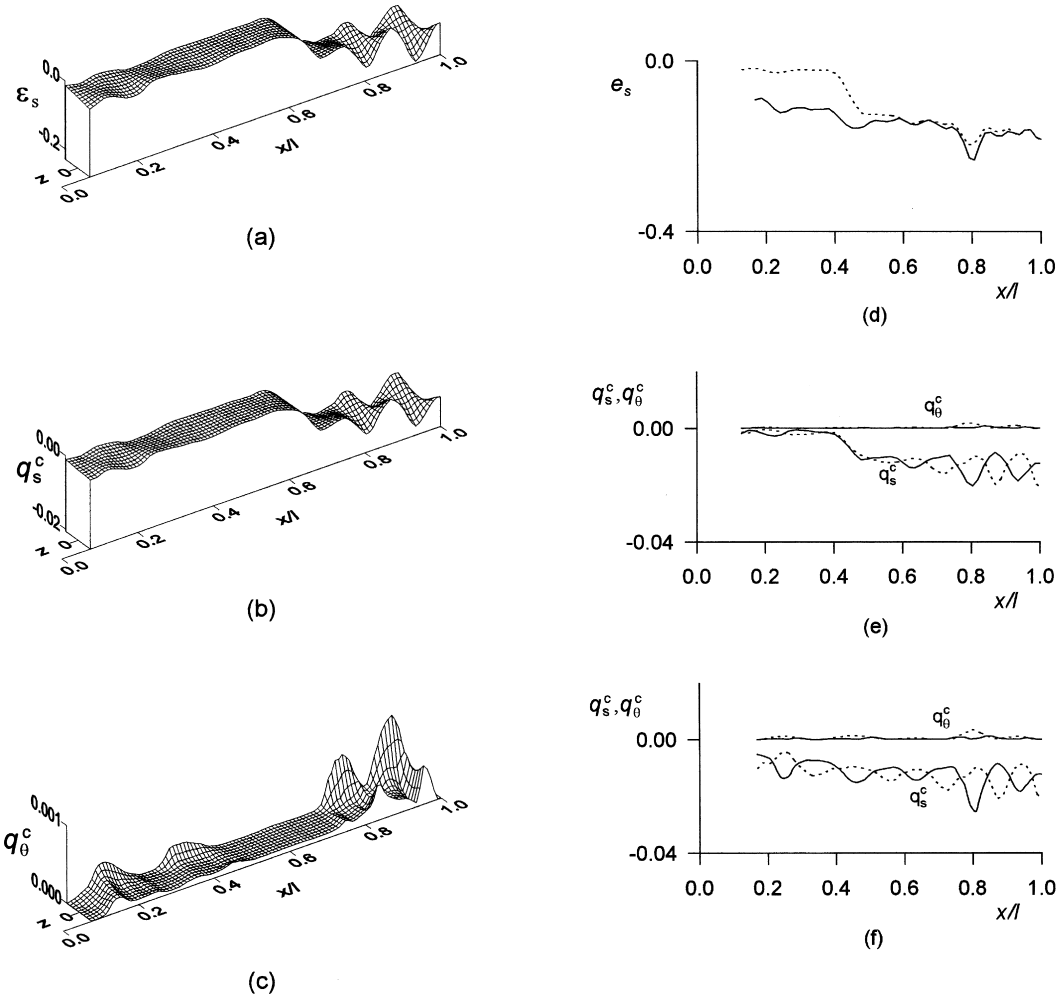

Fig. 8. Stress–strain state of tube 4 (Florence and Goodier, 1968): (a) distribution of the meridional strain, $\varepsilon_s(x, z)$, at $t = 65$ μs; (b) movement of the yield loci, $q_s^c(x, z)$, at $t = 65$ μs; (c) movement of the yield loci, $q_\theta^c(x, z)$, at $t = 65$ μs; (d) mean meridional strain, e_s, --- $t = 100$ μs, — $t = 150$ μs; (e) movement of the yield loci, q_s^c, at $t = 100$ μs, - - - outer surface, — inner surface; (f) movement of the yield loci, q_θ^c, at $t = 150$ μs, - - - outer surface, — inner surface.

The mean meridional strain distributions at $t = 100$ μs and 150 μs are presented in Fig. 8(d) and the movements of the yield loci are presented in Fig. 8(e, f) for the inner ($z = -h/2$) and for the outer ($z = h/2$) shell surfaces, respectively. It is evident that buckling develops with a sustained uniaxial plastic flow and that the radial displacements start to grow at a point as soon as the primary plastic wave has propagated a sufficient distance for a wrinkle to form. The buckling shape is completely formed at $t = 150$ μs (Fig. 7) when the plastic wave, which is propagating at a speed c_1^{p}, has reached the other end of the tube. Subsequently, the reflection of this wave from the end $x = 0$ causes only an increase of the radial displacement amplitudes near this end.

It is shown in Section 4.3 that the deformed shape of a moving specimen impacting on a rigid wall at $v_0 = 81$ m/s and having a thickness $h = 1.65$ mm (Fig. 6(d)) is characterised by large local deformations near the impacted end in contrast with the regular shape of the shell in Fig. 6(c). In the case in

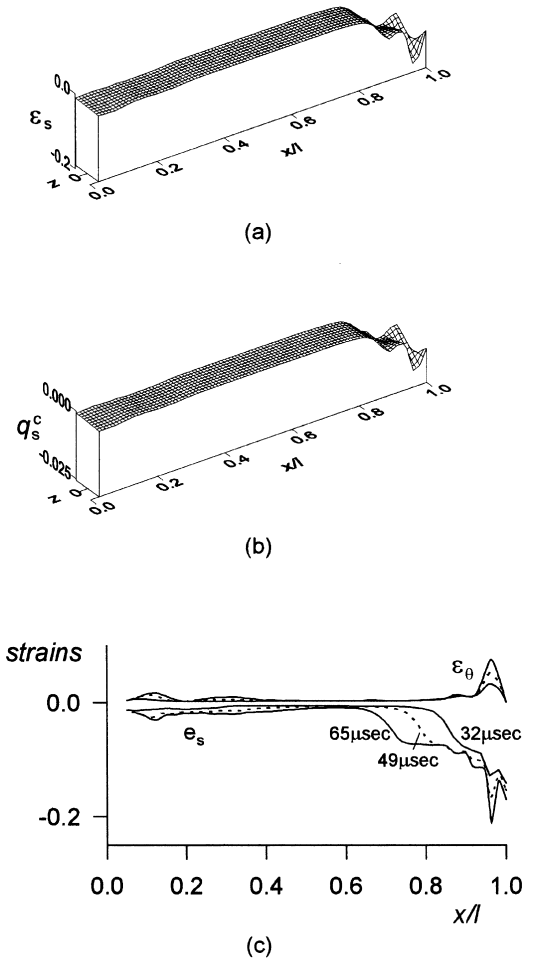

Fig. 9. Stress–strain state of specimen M4 (Murase and Jones 1993) (moving) $n = 50$, $n_t = 3$: (a) distribution of the meridional strain, ε_s (x, z), at $t = 32$ μs; (b) movement of the yield loci, q_s^c (x, z), at $t = 32$ μs; (c) strain distribution at $t = 32$, 49 and 65 μs.

Fig. 6(d), a plastic wave with a speed c_1^p propagates from the impacted end at $t = 0$ and the buckling profile starts to develop as soon as this wave has passed a critical length sufficient for the first wrinkle to develop. The strain distribution and the corresponding origins of the yield loci, q_s^c, are presented at $t = 32$ μs in Figs. 9(a) and 9(b), respectively. The strain distributions at $t = 32$, 49 and 65 μs in Fig. 9(c) show that large plastic deformations, both in compression and bending, develop near the impacted end. The plastic wave originating from this end, however, only propagates from this end until the growth of the radial displacements causes a partial elastic unloading of some cross-sections and a development of reversed plastic loading. Small plastic deformations are evident near the moving end which are caused by the elastic waves being reflected as plastic waves from the attached mass.

5.2. Stress wave phenomena in a stationary specimen

A different pattern of the stress waves is observed when a stationary specimen (Fig. 1(a)) is struck by a small mass travelling with a high initial velocity. The suddenly applied force at the impacted end,

which decreases with time (Fig. 5(b)), causes a plastic wave to propagate along the length of the shell with a decreasing strain amplitude at speed approximately c_1^p (Karagiozova and Jones, 1996b) and the associated strain distribution is shown in Fig. 10(a) at $t = 49\mu$s. The co-ordinates of the centres of the yield loci, q_s^c, and q_θ^c, are presented in Fig. 10(b) and 10(c) and reveal a nearly uniaxial stress state. It is evident, however, that the shell wall has undergone plastic deformations along the entire length which is caused by the faster plastic wave, c_2^p. In a similar manner to the case of a moving specimen described in the previous section, much larger plastic strains are associated with the slower stress wave travelling at speed c_1^p (Fig. 10(a, d)). The slower plastic wave propagates one length of the tube in 189 μs ($\tau = 0.932$), while the corresponding time for the faster plastic wave is 18 μs ($\tau = 0.118$). Although the axial strains near the impacted end are beyond the elastic limit ($\varepsilon_e = \sigma_0/E = 0.0045$) and the corresponding axial stress could cause buckling, the primary plastic wave continues to propagate until $t \approx 50$ μs without buckling because the radial inertia suppresses the growth of the radial displacements. A wrinkle starts to develop from the stationary end due to the elastic wave being reflected as a plastic one. The corresponding strain distributions are shown in Fig. 10(d) and correspond to the buckled profile presented in Fig. 10(e) with small wrinkles along the length and larger radial displacements near the stationary end which are particularly noticeable at $t = 81$ μs. Large plastic strains have developed near the stationary end because this boundary causes a new plastic wave to develop which propagates with a speed c_1^p. For $t > 100$ μs, the primary plastic wave is destroyed and the final buckling shape (Fig. 5(a)) corresponds to the one which develops early in the response (Fig. 10(e)).

The development of the deformation process shows that a regular buckling shape develops during the passage of the primary plastic wave, but that radial inertia suppresses the rapid growth of the radial displacements. The strains almost double upon reflection of the elastic wave at $x = l$ leading to large axial strains near the stationary end. Simultaneously, the circumferential forces increase rapidly which causes a local wrinkle to develop near the stationary end. The stress profiles at some cross-sections at $t = 300$ μs are shown in Fig. 10(f). It is evident that the cross-sections near the stationary end ($x = l$) have undergone large plastic deformations leading to reversed plastic loading, while the rest of the shell has preserved the shape formed during the passage of the primary plastic wave when large compressive strains develop. The observed buckling profile can be attributed to the inertia properties of the striker which cause an initial unloading wave (Nowacki, 1978; Karagiozova and Jones, 1996b) to propagate along the shell, so that only the reflected elastic wave can cause large deformations near the stationary end.

A lower impact velocity requires larger striking masses in order to provide sufficient energy to cause buckling of a stationary specimen. In this case, the critical stress for buckling can be reached after a number of reflections. This phenomenon can be observed for specimen B in Fig. 4(b) ($G = 12.2$ kg, $v_0 = 7$ m/s) which cannot buckle in the elastic range. Thus, axial elastic waves propagate along the shell and reflect from the boundaries until the stresses reach the yield limit. In this particular case, the elastic wave reflects from the moving end as a plastic one at $\tau = 0.19$ ($t \approx 29$ μs) and starts to propagate with a speed c_1^p. Due to the circumferential forces and finite rise time of the applied force, a plastic wave having a speed $c_2^p > c_1^p$ starts to propagate at $t \approx 36$ μs ($\tau = 0.237$) from the same end of the shell. At $t \approx 43$ μs ($\tau = 0.285$), the next reflection of the elastic wave from the stationary end also initiates a plastic wave with a speed c_2^p. This wave has propagated a distance of $0.56l$ from the stationary end at $t = 53$ μs when the entire length of the shell has become plastic. At this particular time the positions of the yield loci (q_s^c and q_θ^c) along the shell and across the thickness are presented in Fig. 11(a) and (b). It is evident that the entire length of the shell has undergone plastic deformations, but with a larger axial compression closer to the stationary end. The positions of the Tresca hexagons, q_s^c and q_θ^c associated with the mid-surface ($z = 0$) are presented for four particular times in Fig. 11(c, d), respectively. These results show that, until $t \approx 53$ μs, the deformation process in the shell can be associated with the stress wave propagation phenomenon, while the structural response governs the deformations for later times.

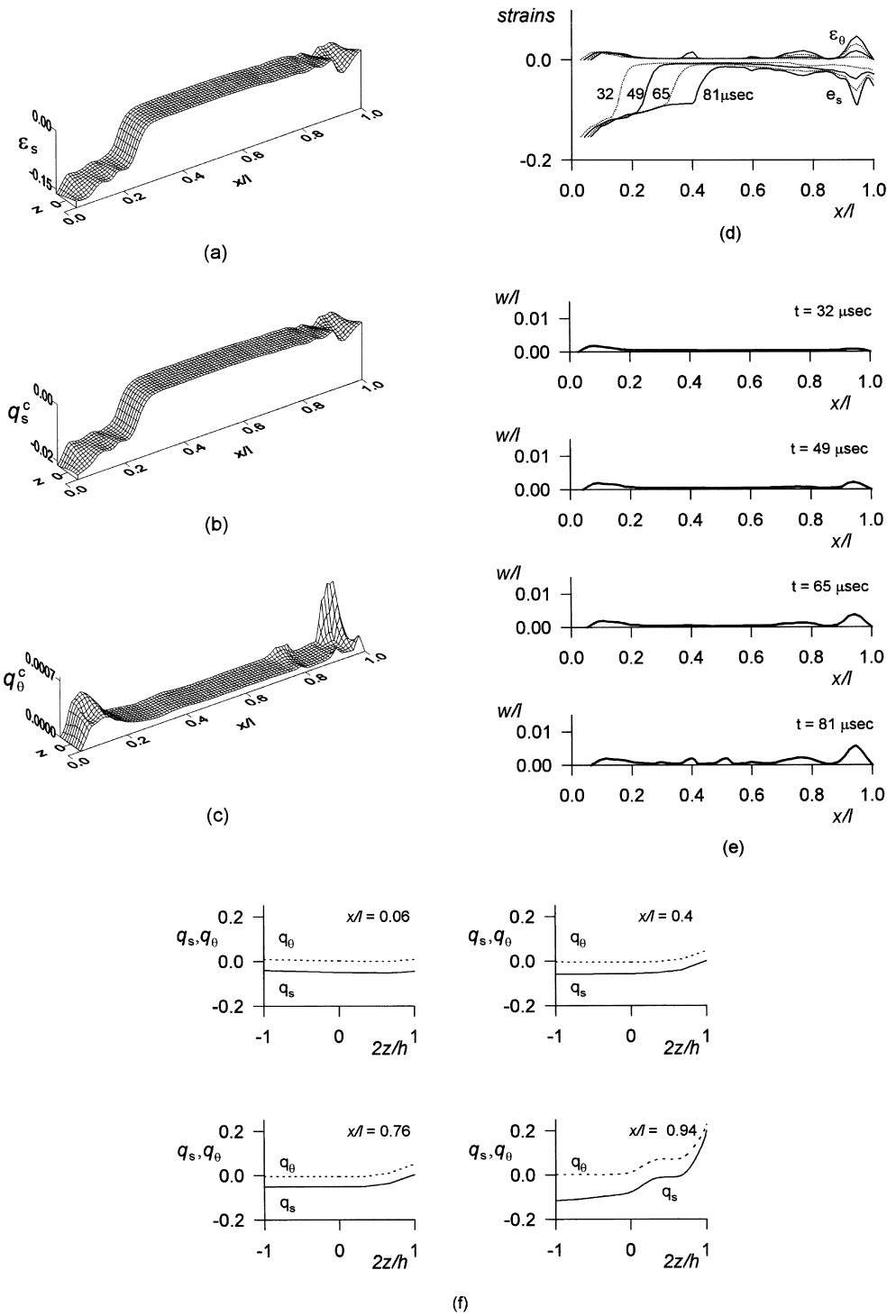

Fig. 10. Stress–strain state of specimen M38 (Murase and Jones, 1993) (stationary) $n = 60$, $n_t = 3$: (a) distribution of the meridional strain, ε_s (x, z), at $t = 49$ μs; (b) movement of the yield loci, q_s^c (x, z), at $t = 49$ μs; (c) movement of the yield loci, q_θ^c (x, z), at $t = 49$ μs; (d) mean meridional strain, e_s and circumferential strain, ε_θ; (e) radial displacement profiles of the shell; (f) stress profiles at $t = 300$ μs.

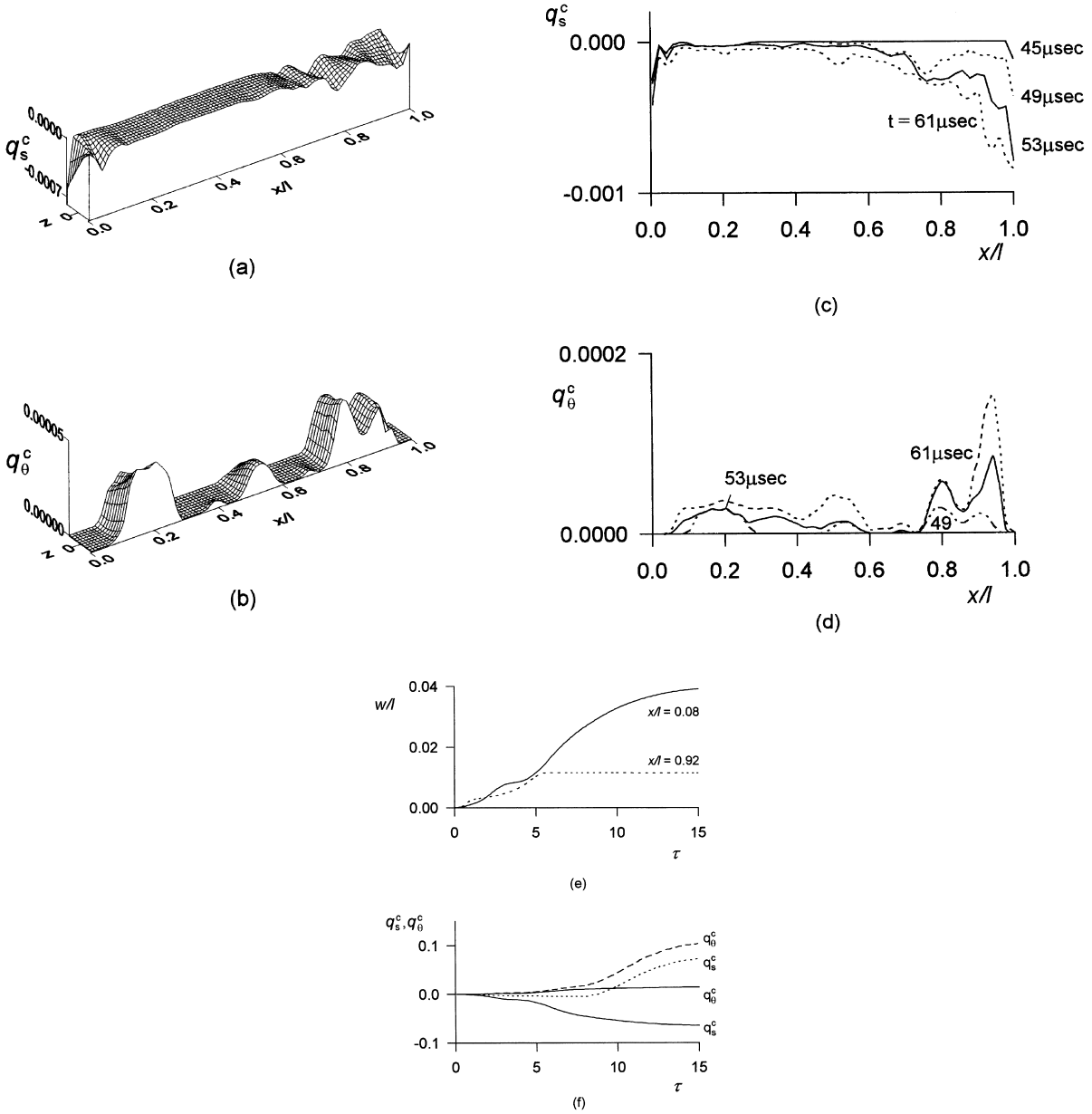

Fig. 11. Behaviour of specimen B; $n = 50$, $n_t = 3$: (a) movement of the yield loci, $q_s^c(x, z)$, at $t = 53$ μs; (b) movement of the yield loci, $q_\theta^c(x, z)$, at $t = 53$ μs; (c) movement of the yield locus, q_s^c, at fibre $z = 0$; (d) movement of the yield locus, q_θ^c, at fibre $z = 0$; (e) variation of the maximum radial displacements with dimensionless time; (f) movement of the yield locus, (q_s^c, q_θ^c) with dimensionless time, - - - outer surface ($z = h/2$); — inner surface ($z = -h/2$).

The plastic deformations, which are associated with the side CD of the yield surface in Fig. 2(c), develop due to the influence of the circumferential forces when the magnitudes of both components q_s and q_θ increase as is shown in Fig. 11(c, d). However, the deformation of the shell develops within a sustained plastic flow under an increasing, almost uniform meridional force until $\tau = 4.7$ ($t \approx 715$ μs). After that, local deformations near the impacted end start to grow more rapidly due to the reduced radial inertia forces.

The temporal variation of the maximum radial displacement near the impacted end (at $x/l = 0.08$) and near the stationary end ($x/l = 0.92$) are shown in Fig. 11(e). The larger stresses near the stationary end at the beginning of the deformation process cause a more rapid growth of the radial displacements near this particular end, but shortly, the radial displacements near the impacted end start to dominate. These displacements start to grow rapidly around $\tau = 4.6$ ($t \approx 700$ μs) which is consistent with the time when the applied force starts to decrease in Fig. 3(b). This behaviour can be explained by the development of the plastic deformations across the thickness of the shell wall. The temporal variation of the yield locus positions associated with the inner ($z = -h/2$) and outer ($z = h/2$) surfaces are shown in Fig. 11(f). The material on the inner surface ($z = -h/2$) is subjected mainly to compression, while a complex loading path is observed for the material on the outer surface. It is evident that the loading path is associated with the side CD until $\tau = 7.6$, but after that, the circumferential forces start to dominate and the loading path is on the side BC when plastic deformations in tension develop and results in large local deflections.

Comparing the force-time histories in Fig. 3(a–c), one can see that the $h = 0.89$ mm thick shell buckles as soon as the stresses reach the critical values because the radial inertia forces cannot support the unbuckled shape. An elastic wave reflects from the stationary end at $\tau = 0.095$ as a plastic wave that results in small local plastic deformations near this particular end. The initial kinetic energy is absorbed largely by the axial compression forces and by the wrinkle, which develops near the impacted end, so that significant deformations in bending do not develop near the stationary end. By way of contrast, the force-time history for the thick 2.41 mm shell has an almost rectangular shape because large radial displacements do not develop during the impact event and cause reversed strains.

5.3. Characteristics of impacts caused by different loading conditions

The results presented in Sections 5.1 and 5.2 demonstrate some of the characteristic features of the axial impact of a cylindrical shell resulting from different loading conditions. The inertia of the striking mass plays an important role in generating the applied axial force and in the development of the strain profile along the longitudinal shell axis at buckling. A large mass–low velocity impact causes mainly a structural response but the stress distribution along the shell at the beginning of the impact event determines the initial buckling shape. High velocity impacts cause different strain distributions at the initiating of buckling. A small striking mass causes a sudden axial loading, which then decreases and initiates an unloading plastic wave (Nowacki, 1978; Karagiozova and Jones, 1996b). However, in spite of the high strains and stresses in the shell, radial inertia suppresses the growth of the radial displacements and only the elastic wave being reflected as a plastic one from the stationary end causes large local radial displacements to develop near this particular end. A primary wave causing a uniform stress and strain arises from an impact on a rigid wall. In this case, the lateral inertia forces in a thicker shell suppress the local growth of the radial displacements, thus allowing for a further propagation of the primary wave and for buckling to develop within a sustained axial compressive plastic flow. A thinner shell subjected to the same loading conditions, however, cannot support the unbuckled shape, so that local deformations grow rapidly near the struck end, thus preventing propagation of the initial plastic stress wave.

The buckling behaviour shows that the radial inertia forces dominate the buckling process. For

example, the deformed shapes presented in Figs. 4(c) and 6(d) are similar geometrically, despite the fact that the loading conditions are completley different, both specimens have buckled near the impacted end, while the remainder of the shell length is deformed slightly. This phenomenon is due to the fact that, in both cases, the radial inertia forces are not large enough to suppress the rapid growth of the radial displacements near an impacted end.

6. Conclusions

The axisymmetric buckling of elastic–plastic circular cylindrical shells under axial impact is studied numerically using a discrete model. A strain-rate insensitive elastic–plastic material with linear strain hardening and displaying the Bauschinger effect is considered. The stress wave propagation effects are analysed for moving and stationary specimens with different loading conditions given by various combinations of the striking mass and the initial velocity. Good agreement is obtained with some experimental data on aluminium alloy tubes.

It is found that the dynamic buckling process is governed by stress wave propagation effects and, in general, the entire length of the shell is involved in the deformation process for a high velocity impact. This phenomenon is known as dynamic plastic buckling. However, the final buckling shape depends strongly on the inertia properties of the striker and the geometry of a shell. Regular buckling shapes for a high velocity impact occur in relatively thick shells when buckling develops within a sustained axial compressive plastic flow. A localisation of buckling can develop in thinner shells when the buckling process involves a partial unloading of some cross-sections of a shell, thereby interrupting any further axial stress wave propagation. A low mass–high velocity impact causes a large axial compression to develop near the impacted end, while large bending deformations occur near the stationary end, and a considerable portion of the initial kinetic energy is absorbed in compression during the initial deformation phase. Larger mass–lower initial velocity impacts tend to cause large bending deformations near the impacted end which leads to a progressive folding.

Acknowledgements

This study has been supported partially by the Royal Society, London, the Impact Research Centre at the University of Liverpool and the Bulgarian NRF through the Contract MM 517/95. The authors wish to thank Ms C. Jones and Mr P. Smith from the Impact Research Centre for the experiments on low velocity impact, which are reported in Section 4.1. The authors are grateful to Prof. R.J. Clifton, Brown University, for some early discussion on Appendix C.

Appendix A. Coefficients in the equation of motion and the boundary conditions

The coefficients in the equations of motion eqn (1b) and (1c) are functions of the angles of rotation φ_i and their particular expressions are

$$a_1 = 2\sin\alpha_{i-1}\Big\{\sin\varphi_i\big[\sin\alpha_{i-1}\big(1+\sin^2\alpha_i\big)+\cos\alpha_{i-1}\sin\alpha_i\cos\alpha_i\big] + \cos\varphi_i\big[\cos\alpha_{i-1}\big(1+\cos^2\alpha_i\big)+\sin\alpha_{i-1}\sin\alpha_i\cos\alpha_i\big]\Big\}^{-1}, \tag{A1a}$$

$$a_2 = 2\sin\alpha_i\Big\{\sin\varphi_{i+1}\big[\sin\alpha_i\big(1+\sin^2\alpha_{i+1}\big)+\cos\alpha_i\sin\alpha_{i+1}\cos\alpha_{i+1}\big] + \cos\varphi_{i+1}\big[\cos\alpha_i\big(1+\cos^2\alpha_{i+1}\big)+\sin\alpha_i\sin\alpha_{i+1}\cos\alpha_{i+1}\big]\Big\}^{-1}, \tag{A1b}$$

$$b_1 = \sin\alpha_i\big(\sin\alpha_i\sin\varphi+\cos\alpha_i\cos\varphi_i\big), \tag{A2a}$$

$$b_2 = \sin\alpha_i\big(\sin\alpha_i\sin\varphi_i+\cos\alpha_i\cos\varphi_i\big), \tag{A2b}$$

$$c_i = \Big\{\sin\varphi_i\big[\sin\alpha_i\big(1+\sin^2\alpha_{i-1}\big)+\cos\alpha_i\sin\alpha_{i-1}\cos\alpha_{i-1}\big]+\cos\varphi_i\big[\cos\alpha_i\big(1+\cos^2\alpha_{i-1}\big) + \sin\alpha_i\sin\alpha_{i-1}\cos\alpha_{i-1}\big]\Big\}\Big/\Big\{\sin\varphi_{i+1}\big[\sin\alpha_i\big(1+\sin^2\alpha_{i+1}\big)+\cos\alpha_i\sin\alpha_{i+1}\cos\alpha_{i+1}\big] + \cos\varphi_{i+1}\big[\cos\alpha_i\big(1+\cos^2\alpha_{i+1}\big)+\sin\alpha_i\sin\alpha_{i+1}\cos\alpha_{i+1}\big]\Big\}, \tag{A3}$$

$$d_1 = \sin\alpha_{i+1}\big(\sin\alpha_{i+1}\sin\varphi_{i+1}+\cos\alpha_{i+1}\cos\varphi_{i+1}\big), \tag{A4a}$$

$$d_2 = \cos\alpha_{i+1}\big(\sin\alpha_{i+1}\sin\varphi_{i+1}+\cos\alpha_{i+1}\cos\varphi_{i+1}\big), \tag{A4b}$$

$$e_1 = \sin\alpha_{i-1}\big(\sin\alpha_{i-1}\sin\varphi_i+\cos\alpha_{i-1}\cos\varphi_i\big), \tag{A5a}$$

$$e_2 = \cos\alpha_{i-1}\big(\sin\alpha_{i-1}\sin\varphi_i+\cos\alpha_{i-1}\cos\varphi_i\big), \tag{A5b}$$

$$s_1 = 2-\Big\{a_1\big[\big(\sin\varphi_i-2b_1\big)+\big(\sin\varphi_i+b_1\big)\sin\varphi_i\big] + 2\sin\varphi_i+a_2\sin\varphi_{i+1}\big[1+\big(\sin\varphi_{i+1}+d_1\big)\big]\Big\}/2 \tag{A6a}$$

$$s_2 = \Big\{(\cos\varphi_i+e_2)+\big(\sin\varphi_i-e_1\big)\sin\varphi_i\cos\varphi_i+c_i\big[\big(\cos\varphi_{i+1}+d_2\big) + \big(\sin\varphi_{i+1}-d_1\big)\sin\varphi_{i+1}\cos\varphi_{i+1}\big]\Big\}/2. \tag{A6b}$$

The functions f_1 and f_2 in eqns (1b) and (1c) present the contribution of the velocities and the accelerations of the neighbouring links of the model to the motion of the i-th cell as

$$
\begin{aligned}
f_1 = {} & \ddot{u}_{i-1}\Big\{a_1 \sin\varphi_i + \big[a_1(\sin\varphi_i + b_1) - 2\big]\sin^2\varphi_i\Big\}/2 \\
& + \ddot{u}_{i+1}\Big\{a_2\Big[\sin\varphi_{i+1} + (\sin\varphi_{i+1} + d_1)\sin^2\varphi_{i+1} - d_1\Big]\Big\}/2 + \ddot{w}_i\Big\{a_1(\cos\varphi_i - b_2) \\
& + \big[a_1(\sin\varphi_i + b_1) - 2\big]\sin\varphi_i\cos\varphi_i + a_2\big[(\cos\varphi_{i+1} - d_2) \\
& + (\sin\varphi_{i+1} + d_1)\sin\varphi_{i+1}\cos\varphi_{i+1}\big]\Big\}/2 - \ddot{w}_{i-1}\big\{a_1(\cos\varphi_i + b_2) \\
& + \big[a_1(\sin\varphi_i + b_1) - 2\big]\sin\varphi_i\cos\varphi_i\big\} - \ddot{w}_{i+1}a_2\big\{\big[(\cos\varphi_{i+1} - d_2) \\
& + (\sin\varphi_{i+1} + d_1)\sin\varphi_{i+1}\cos\varphi_{i+1}\big]\big\}/2 + \big[(\dot{w}_i - \dot{w}_{i-1})\cos\varphi_i \\
& + (\dot{u}_{i-1} - \dot{u}_i)\sin\varphi_i\big]^2\cos\varphi_i\big[a_1(\sin\varphi_i + b_1) - 2\big]/2L_i + \big[(\dot{w}_{i+1} - \dot{w}_i)\cos\varphi_{i+1} \\
& + (\dot{u}_i - \dot{u}_{i+1})\sin\varphi_{i+1}\big]^2\cos\varphi_{i+1}(\sin\varphi_{i+1} + d_1)a_2/2L_{i+1},
\end{aligned}
\tag{A7a}
$$

$$
\begin{aligned}
f_2 = {} & \ddot{u}_i\Big\{2e_2 + \sin\varphi_i + (\sin\varphi_i - e_1)\sin^2\varphi_i + c_i\sin\varphi_{i+1}\big[1 + \sin\varphi_{i+1}(\sin\varphi_{i+1} + d_1)\big]\Big\}/2 \\
& - \ddot{u}_{i-1}\sin\varphi_i\big[1 + \sin\varphi_i(\sin\varphi_i - e_1)\big]/2 + \ddot{u}_{i+1}c_i\Big[2d_1 - \sin\varphi_{i+1} \\
& + (\sin\varphi_{i+1} + d_1)\sin^2\varphi_{i+1}\Big]/2 + \ddot{w}_{i-1}\big[(\cos\varphi_i - e_2) \\
& + (\sin\varphi_i - e_1)\sin\varphi_i\cos\varphi_i\big]/2 + \ddot{w}_{i+1}c_i\big[(\cos\varphi_{i+1} - d_2) \\
& + (\sin\varphi_{i+1} + d_1)\sin\varphi_{i+1}\cos\varphi_{i+1}\big]/2 + \big[(\dot{w}_i - \dot{w}_{i-1})\cos\varphi_i \\
& + (\dot{u}_{i-1} - \dot{u}_i)\sin\varphi_i\big]^2\cos\varphi_i(\sin\varphi_i - e_1)/2L_i \\
& + \big[(\dot{w}_{i+1} - \dot{w}_i)\cos\varphi_{i+1} + (\dot{u}_i - \dot{u}_{i+1})\sin\varphi_{i+1}\big]^2\cos\varphi_{i+1}(\sin\varphi_{i+1} + d_1)c_i/2L_{i+1}.
\end{aligned}
\tag{A7b}
$$

The equations of motion for w_1, w_{n-1} and u_n incorporate the particular boundary conditions, so that in the lateral direction they are

$$
\begin{aligned}
s_2 m L_1\ddot{w}_1 = {} & M_0^s - M_1^s(1 + c_1L_1/L_2) + M_2^s c_1L_1/L_2 - N_0^s L_1\cos\big(\varphi_1/2\big)\sin\varphi_1/2 \\
& + N_2^s L_1 c_1\big[\cos\alpha_2(\sin\varphi_2 - d_1) - \sin\alpha_2(\cos\varphi_2 - d_2)\big]/2 - N_1^s L_1\big\{\cos\alpha_1\big[\sin\varphi_1 - c_1(\sin\varphi_2 \\
& + d_1)\big] - \sin\alpha_1\big[\cos\varphi_2 - c_1(\cos\varphi_2 + d_2)\big]\big\}/2 - N_1^r L_1\big[(\cos\varphi_1 + c_1(\cos\varphi_2 + d_2)/2)\big]/2 \\
& + N_2^r L_1 c_1(\cos\varphi_2 - d_2)/4 + mL_1 f_2(\ddot{w}_{21}, \ddot{u}_0, \ddot{u}_1, \ddot{u}_2, \dot{w}_1, \dot{w}_2, \dot{u}_0, \dot{u}_1, \dot{u}_2),
\end{aligned}
\tag{A8a}
$$

where

$$c_1 = \left(\sin\alpha_1 \sin\varphi_1 + 2\cos\alpha_1 \cos\varphi_1\right)/\Big\{\sin\varphi_2\left[\sin\alpha_1\left(1 + \sin^2\alpha_2\right) + \cos\alpha_1 \sin\alpha_2 \cos\alpha_2\right] + \cos\varphi_2\left[\cos\alpha_1\left(1 + \cos^2\alpha_2\right) + \sin\alpha_1 \sin\alpha_2 \cos\alpha_2\right]\Big\}$$

and

$$\begin{aligned} s_2 m L_n \ddot{w}_{n-1} = {} & M_n^s - M_{n-1}^s(1 + c_n L_n/L_{n-1}) + M_{n-2}^s c_n L_n/L_{n-1} - N_{n-2}^s L_n c_n\left[\cos\alpha_{n-2}\left(\sin\varphi_{n-1} - d_1\right)\right. \\ & \left. - \sin\alpha_{n-2}\left(\cos\varphi_{n-1} - d_2\right)\right]/2 + N_n^s L_n \cos\left(\varphi_n/2\right)\sin\varphi_n/2 - N_{n-1}^s L_n\left\{\cos\alpha_i\left[\sin\varphi_n - c_n\left(\sin\varphi_{n-1}\right.\right.\right. \\ & \left.\left.\left. + d_1\right)\right] - \sin\alpha_i\left[\cos\varphi_n - c_n\left(\cos\varphi_{n-1} + d_2\right)\right]\right\}/2 + N_{n-2}^r L_n\left(\cos\varphi_{n-1} - d_2\right)/4 - N_{n-1}^r L_n\left[\cos\varphi_n \right. \\ & \left. + c_n\left(\cos\varphi_{n-1} + d_2\right)/2\right]/2 + m L_n f_2(\ddot{w}_{n-2}, \ddot{u}_{n-2}, \ddot{u}_{n-1}, \ddot{u}_n, \dot{w}_{n-2}, \dot{w}_{n-1}, \dot{u}_{n-2}, \dot{u}_{n-1}, \dot{u}_n), \end{aligned} \tag{A8b}$$

where

$$c_n = \Big\{\sin\varphi_n\left[\sin\alpha_n\left(1 + \sin^2\alpha_{n-1}\right) + \cos\alpha_n \sin\alpha_{n-1}\cos\alpha_{n-1}\right] + \cos\varphi_n\left[\cos\alpha_n\left(1 + \cos^2\alpha_{n-1}\right) + \sin\alpha_n \sin\alpha_{n-1}\cos\alpha_{n-1}\right]\Big\}/\left(\sin\alpha_{n-1}\sin\varphi_n + 2\cos\alpha_{n-1}\cos\varphi_n\right)$$

The equation of motion of the n-th link of the model in the axial direction is

$$\begin{aligned} s_1 m \ddot{u}_n = {} & N_n^s \cos\left(\varphi_n/2\right)\left(1 + a_1 \sin\varphi_n\right) - N_{n-1}^s\left[\cos\alpha_{n-1}\left(2 - a_1\sin\varphi_n\right) + a_1 \sin\alpha_{n-1}\cos\varphi_n\right]/2 \\ & - N_{n-1}^r a_1 \cos\varphi_n/2 - a_1\left(M_{n-1}^s - M_n^s\right)/L_n + m f_1(\ddot{w}_{n-1}, \ddot{u}_{n-1}, \dot{w}_{n-1}, \dot{u}_{n-1}, \dot{u}_n) + 2mg, \end{aligned} \tag{A8c}$$

where

$$s_1 = 2 + \cos\varphi_n\left[2a_1 - \left(a_1\sin\varphi_n - 2\right)\sin\varphi_n\right].$$

Appendix B. Constitutive relations for elastic–plastic media in a plane stress state obeying Tresca's yield condition

The equivalent stress for the Tresca criterion in terms of principal stresses in a plane stress state is

$$\bar{\sigma} = \sigma_1 - \sigma_3 \tag{B1}$$

where σ_1 and σ_3 are the maximum and the minimum principal stresses. The flow rules associated with Tresca yield criterion depend on the particular loading regime (Mendelson, 1972) which is represented by the sides of the diagram in Fig. 2(c). Neglecting the shear stresses, the flow rules for a material having a linear strain hardening can be obtained as functions of $\mathrm{d}\sigma_s$ and $\mathrm{d}\sigma_\theta$. For sides AB and DE

$$\mathrm{d}\varepsilon_s^p = \frac{\sqrt{3}}{2H'}\,\mathrm{d}\sigma_s, \quad \mathrm{d}\varepsilon_\theta^p = 0, \ \mathrm{d}\varepsilon_z^p = -\mathrm{d}\varepsilon_s^p \tag{B2a)–(B2c}$$

when taking into account eqn (6) and $\mathrm{d}\bar{\sigma} = |\mathrm{d}\sigma_s|$. The strain increments associated with sides BC and EF are

$$d\varepsilon_s^p = 0, \quad d\varepsilon_\theta^p = \frac{\sqrt{3}}{2H'}\, d\sigma_\theta, \quad d\varepsilon_z^p = -d\varepsilon_\theta^p \tag{B3a–B3c}$$

when $d\bar{\sigma} = |d\sigma_\theta|$. The corresponding relationships between the stress increments and the plastic strain increments are

$$d\varepsilon_s^p = -\frac{\sqrt{3}}{2H'}(d\sigma_\theta - d\sigma_s), \quad d\varepsilon_\theta^p = \frac{\sqrt{3}}{2H'}(d\sigma_\theta - d\sigma_s), \quad d\varepsilon_z^p = 0, \tag{B4a–B4c}$$

on side CD when $d\bar{\sigma} = d\sigma_\theta - d\sigma_s$, and

$$d\varepsilon_s^p = \frac{\sqrt{3}}{2H'}(d\sigma_s - d\sigma_\theta), \quad d\varepsilon_\theta^p = -\frac{\sqrt{3}}{2H'}(d\sigma_s - d\sigma_\theta), \quad d\varepsilon_z^p = 0, \tag{B5a–B5c}$$

on side AF when $d\bar{\sigma} = d\sigma_s - d\sigma_\theta$.

Explicit expressions for the stress increments as functions of the strain increments and the material properties, and associated with each side of the Tresca diagram, can be obtained using eqns (B2)–(B5) as

$$d\sigma_s = 2\lambda E(d\varepsilon_s + \nu d\varepsilon_\theta)\left[(1-\lambda)\sqrt{3} + 2\lambda(1-\nu^2)\right]^{-1}, \tag{B6a}$$

$$d\sigma_\theta = 2\lambda E\left\{2\lambda\nu\, d\varepsilon_s + \left[(1-\lambda)\sqrt{3} + 2\lambda\right]d\varepsilon_\theta\right\}\left[(1-\lambda)\sqrt{3} + 2\lambda(1-\nu^2)\right]^{-1} \tag{B6b}$$

for loading paths from the sides AB or DE,

$$d\sigma_s = 2\lambda E\left\{\left[(1-\lambda)\sqrt{3} + 2\lambda\right]d\varepsilon_s + 2\lambda\nu\, d\varepsilon_\theta\right\}\left[(1-\lambda)\sqrt{3} + 2\lambda(1-\nu^2)\right]^{-1} \tag{B7a}$$

$$d\sigma_\theta = 2\lambda E(\nu\, d\varepsilon_s + d\varepsilon_\theta)\left[(1-\lambda)\sqrt{3} + 2\lambda(1-\nu^2)\right]^{-1} \tag{B7b}$$

for loading paths from sides BC or EF and

$$d\sigma_s = \frac{E}{2(1-\nu)\left[(1-\lambda)\sqrt{3} + \lambda(1+\nu)\right]}\left\{\left[(1-\lambda)\sqrt{3} + 2\lambda\right]d\varepsilon_s + \left[(1-\lambda)\sqrt{3} + 2\lambda\nu\right]d\varepsilon_\theta\right\}, \tag{B8a}$$

$$d\sigma_\theta = \frac{E}{2(1-\nu)\left[(1-\lambda)\sqrt{3} + \lambda(1+\nu)\right]}\left\{\left[(1-\lambda)\sqrt{3} + 2\lambda\nu\right]d\varepsilon_s + \left[(1-\lambda)\sqrt{3} + 2\lambda\right]d\varepsilon_\theta\right\}, \tag{B8b}$$

for the loading path from sides CD or AF. It is evident that in the case of elastic loading and elastic unloading ($\lambda = 1$) eqns (B6)–(B8) give the wholly elastic stress increments

$$d\sigma_s = E(d\varepsilon_s + \nu\, d\varepsilon_\theta)/(1-\nu^2) \tag{B9a}$$

$$d\sigma_\theta = E(\nu\, d\varepsilon_s + d\varepsilon_\theta)/(1-\nu^2). \tag{B9b}$$

Appendix C. Wave speeds in elastic–plastic media obeying Tresca's yield condition

Consider a thin-walled tube made of an elastic–plastic rate insensitive material with linear strain

hardening and subjected to an axial loading. It is assumed that the radial displacements are small, so that the meridional s-axis coincides with the x-axis. The biaxial stress state $\sigma_s \neq 0, \sigma_\theta \neq 0$ is assumed to obey the Tresca yield condition in Fig. 2(c). The corresponding constitutive equations may be written in the form

$$\dot{\varepsilon}_x = A_1\dot{\sigma}_x + A_2\dot{\sigma}_\theta \tag{C1a}$$

$$\dot{\varepsilon}_\theta = A_2\dot{\sigma}_x + A_3\dot{\sigma}_\theta \tag{C1b}$$

where A_1, A_2, A_3 have different values depending on the side of the Tresca hexagon, namely

$$A_1 = \frac{1}{E} + \frac{\sqrt{3}}{2H'}, \quad A_2 = -\frac{\nu}{E} \quad \text{and} \quad A_3 = \frac{1}{E} \tag{C2a}$$

are associated with sides AB and DE,

$$A_1 = \frac{1}{E}, \quad A_2 = -\frac{\nu}{E} \quad \text{and} \quad A_3 = \frac{1}{E} + \frac{\sqrt{3}}{2H'} \tag{C2b}$$

are associated with sides BC and EF and

$$A_1 = A_3 = \frac{1}{E} + \frac{\sqrt{3}}{2H'} \quad \text{and} \quad A_2 = -\frac{\nu}{E} - \frac{\sqrt{3}}{2H'} \tag{C2c}$$

are associated with sides CD and FA, respectively. The small strain kinematic equations may be written as

$$\dot{\varepsilon}_x = v_{x,x} \tag{C3a}$$

$$\dot{\varepsilon}_\theta = \frac{1}{a}v_r, \tag{C3b}$$

where the comma denotes differentiation with respect to the subsequent variable and $v_x = \partial u/\partial t$, $v_r = \partial w/\partial t$ are the corresponding particle velocities. The equations of motion are given by

$$\sigma_{x,x} = \rho\dot{v}_x, \tag{C4a}$$

$$-\sigma_0 = \rho\dot{v}_r, \tag{C4b}$$

where ρ is the material density.

The strain rates can be eliminated from eqns (C1)–(C3) to give two equations involving only stresses and velocities, which, together with the equations of motion, can be written in a matrix form

$$\boldsymbol{A}^t\boldsymbol{w}_{,t} + \boldsymbol{A}^x\boldsymbol{w}_{,x} + \boldsymbol{b} = 0, \tag{C5a,b}$$

where

$$\boldsymbol{w}=\begin{bmatrix}\dot{u}\\ \sigma_x\\ \dot{w}\\ \sigma_\theta\end{bmatrix},\quad \boldsymbol{A}^t=\begin{bmatrix}\rho & 0 & 0 & 0\\ 0 & A_1 & 0 & A_2\\ 0 & 0 & \rho a & 0\\ 0 & A_2 & 0 & A_3\end{bmatrix},\quad \boldsymbol{A}^x=\begin{bmatrix}0 & -1 & 0 & 0\\ -1 & 0 & 0 & 0\\ 0 & 0 & 0 & 0\\ 0 & 0 & 0 & 0\end{bmatrix},\quad \boldsymbol{b}=\begin{bmatrix}0\\ 0\\ -\sigma_\theta\\ -\dot{w}/a\end{bmatrix}. \tag{C6a–C6d}$$

Acceleration waves propagate at speeds 'c_1' which are the roots of

$$|-c_1\boldsymbol{A}^t+\boldsymbol{A}^x|=0 \tag{C7a}$$

or

$$-\rho^2 a\left(A_2^2-A_1A_3\right)c_1^4-\rho a A_3 c_1^2=0 \tag{C7b}$$

and for $c_1\neq 0$ the acceleration wave speed is

$$c_1=\pm\left\{A_3/\left[\rho\left(A_1A_3-A_2^2\right)\right]\right\}^{1/2}. \tag{C8}$$

For the particular piece-wise linear yield surface in Fig. 2(c), three different plastic wave speeds can exist. The speeds associated with sides AB and DE are

$$c_1^{\mathrm{p}}=\pm(E/\rho)^{1/2}\left\{2\lambda/\left[2\lambda(1-\nu^2)+(1-\lambda)\sqrt{3}\right]\right\}^{1/2}, \tag{C9a}$$

the speeds associated with sides CD and FA are

$$c_2^{\mathrm{p}}=\pm(E/\rho)^{1/2}\left\{\frac{2\lambda+(1-\lambda)\sqrt{3}}{2(1-\nu)\left[\lambda(1+\nu)+(1-\lambda)\sqrt{3}\right]}\right\}^{1/2}, \tag{C9b}$$

while the speeds associated with sides BC and EF are

$$c_3^{\mathrm{p}}=\pm(E/\rho)^{1/2}\left\{\frac{2\lambda+(1-\lambda)\sqrt{3}}{2\lambda(1-\nu^2)+(1-\lambda)\sqrt{3}}\right\}^{1/2} \tag{C9c}$$

It is evident that the acceleration wave speeds for elastic loading or unloading ($\lambda=1$) given by eqns (C9a–c) are identical and equal to

$$c^{\mathrm{e}}=\pm(E/\rho)^{1/2}(1-\nu^2)^{-1/2}. \tag{C9d}$$

The plastic wave speeds, c^{p}, depend on the hardening modulus, E_{h}, and on the loading path. The particular calculations show that the waves' speeds, c_1^{p}, associated with the parts of the Tresca hexagon having only one plastic strain rate different from zero (i.e. sides AB and DE) are very close to the uniaxial plastic wave in a rod being equal to $c_1^{\mathrm{p}}\approx\pm 1.07(\lambda E/\rho)^{1/2}$ for $\nu=0.3$. The plastic waves associated with the sides CD and FA are characterised by two plastic strain rate components, $\dot{\varepsilon}_x$, $\dot{\varepsilon}_\theta$, can propagate with much larger velocities, e.g. $c_2^{p}\approx\pm 0.86(E/\rho)^{1/2}$ for $\nu=0.3$ and $E_{\mathrm{h}}/E\in(0.005, 0.05)$, typical for metals. A general discussion on the wave speeds in elastic–plastic media obeying Tresca's yield condition can be found in Ting (1976).

References

Benson, D.J., Hallquist, J.O., 1990. A single surface contact algorithm for the post buckling analysis of shell structures. Computer Methods in Applied Mechanics and Engineering 78, 141–163.

Chen Changen, Su Xianyue, Han Mingbao, Wang Ren, 1992. Elastic–plastic dynamic buckling and the stress wave in cylindrical shells subjected to axial impact. In: Proceedings of the International Symposium Intense Dynamic Loading and Its Effects, Chengdu, China, 9–12 June, 543–546.

Florence, A.L., Goodier, J.N., 1968. Dynamic plastic buckling of cylindrical shells in sustained axial compressive flow. Journal of Applied Mechanics March, 80–86.

Jones, N., 1989. Structural Impact. Cambridge University Press (Paperback edition, 1997).

Karagiozova, D., Jones, N., 1996a. Multi-degrees of freedom model for dynamic buckling of an elastic–plastic structure. International Journal of Solids and Structures 33, 3377–3398.

Karagiozova, D., Jones, N., 1996b. Dynamic elastic–plastic buckling phenomena in a rod due to axial impact. International Journal of Impact Engineering 18, 919–947.

Lee, L.H.N., 1981a. Flexural waves in rods within an axial compressive wave. Wave Motion 3, 243–255.

Lee, L.H.N., 1981b. Dynamic buckling of inelastic column. International Journal of Solids and Structures 17, 413–418.

Lepik, U., 1998. On plastic buckling of cylindrical shells struck axially with a mass. International Journal of Non-Linear Mechanics 33, 235–246.

Li Ming, Wang Ren, Han Mingbao, 1994. An experimental investigation of the dynamic axial buckling of cylindrical shells using a Kolsky bar. Acta Mechanica Sinica 10, 260–266.

Mendelson A., 1972. Plasticity: Theory and Applications. The Macmillan Company, New York, Collier–Macmillan Limited, London.

Murase, K., Jones, N., 1991. The transition from progressive plastic buckling to dynamic plastic buckling. Report of the Faculty of Science and Technology, Meijo University, Nagoya, Japan, pp. 81–87.

Murase, K., Jones, N., 1993. The variation of modes in the dynamic axial plastic buckling of circular tubes. In: Gupta, N.K. (Ed.). Plasticity and Impact Mechanics. Wiley Eastern Limited, pp. 222–237.

Nowacki, W.K., 1964. Stress-Waves in Non-Elastic Solids. Pergamon Press, UK.

Sewell, M.J., 1973. A yield-surface corner lowers the buckling stress of an elastic–plastic plate under compression. Journal of the Mechanics and Physics of Solids 21, 19–45.

Ting, T.C.T., 1976. Wave speeds and slowness surface in elastic–plastic media obeying Tresca's yield condition. In: Proceedings of the 13th Annual Meeting of the Society of Engineering Science, NASA/CP-2001, 85–94.

Wang Ren, Han Mingbao, Huang Zhuping, Yan Qingchun, 1983. An experimental study on the dynamic axial plastic buckling of cylindrical shell. International Journal of Impact Engineering 1, 249–256.